Stochastic modelling of crack propagation in materials with random properties using isometric mapping for dimensionality reduction of nonlinear data sets

***M. Mousavi Nezhad[1], E. Gironacci[1], M. Rezania[1] and N. Khalili[2]**

[1]School of Engineering, University of Warwick, Coventry, United Kingdom

[2]School of Civil and Environmental Engineering, University of New South Wales, Sydney, Australia

*m.mousavi-nezhad@warwick.ac.uk

ABSTRACT

Fractures tend to propagate along the least resistance paths, and homogeneous-based models may not be able to reliably predict the true crack paths, as they are not capable of capturing nonlinearities and local damage induced by local inhomogeneity. This paper presents a stochastic numerical modelling framework for simulating fracturing in natural heterogeneous materials. Fracture propagation is modelled using Francfort and Marigo's variational theory, and randomness in the material properties is introduced by random field principle. A computational strategy on the basis of nonlinear dimensionality reduction framework is developed that maps domain of spatially variable properties of the materials to a low-dimensional space. This strategy allows us to predict the most probable fracture patterns leading to failure by an optimisation algorithm. The reliability and performance of the developed methodology are examined through simulation of experimental case studies and comparison of predictions with measured data.

Key Words: *stochastic damage modelling, heterogeneous materials, crack propagation, nonlinear dimensionality reduction*

1. Introduction

Practice reveals that the presence of heterogeneous structure, enclosed joints, micro-cracks, natural discontinuities and laminations can significantly affect the strength and failure mechanism of a material. In recent years, many researchers have focused on the problem of modelling heterogeneous materials containing discontinuities.

Multi-scale methods have offered a significant progress in description of the effects of microscale heterogeneity of the materials on their macroscale behaviour [1]. Heterogeneous structures, like concrete, rocks or composites, often need a finer scale determination of micro effects influencing the macroscopic mechanical response [2]. Several mechanical frameworks and corresponding numerical models have been proposed and implemented on the basis of the multi-scale method. However, applicability of the method is restricted to scenarios where a detailed knowledge of material microstructure is available.

An increasing interest is therefore spreading to stochastic approaches, as they allow to probabilistically determine the degree of the material heterogeneity, through quantifying fluctuations of the mechanical properties, geometry, loading and boundary conditions [3-6]. Through this approach, the treatment of the uncertainties in the heterogeneous material response is achieved by means of probability principles and statistics, such as stochastic approaches, as the effect of uncertainties cannot be properly addressed by using conventional deterministic approaches.

In addition to the need for a sound theory for microstructural description of material properties and comprehensive uncertainty analysis of the fracturing structures involving material properties randomness, a numerically compatible and efficient computational strategy is essential to predict evolution of discontinuity.

In the context of the finite element method, modelling of discontinuities has been conducted with different approaches which can be categorised into two main groups: discrete or smeared approaches. The discrete approach [7], identifies the new cracks as localised newly-emerged boundaries of the bulk material; while, the smeared approach [8], looks at cracks by incorporating strain or displacement discontinuities into standard finite-element interpolations [9].

Cohesive crack methodology has been widely used by many researchers for stochastic analyses of fracture propagation e.g., [10-12], in which cohesive elements are inserted between element edges. If crack paths are unknown a priori, local r-adaptivity and mesh-realignment techniques are required to resolve mesh dependency issues [13]. This can lead to

high computational cost, particularly if Monte Carlo (MC) simulation approach is employed. Few frameworks have been proposed in the context of the continuum approaches and smeared crack models to study the stochastic aspect of the failure. These frameworks which rely on the basis of non-local damage theory and mesh refinement algorithms to resolve mesh sensitivity of numerical solutions, suffer from some restrictions due to the complexities in introduction of an internal length scale in the continuum with spatially correlated random properties [14]. The key issue is, if fine mesh is used around crack tips for discretization of continuous random field, it may cause near perfect correlation between variables resulting in numerical instability [15], while a coarse discretization may result in overlapping important data features onto the same sample portion of the field or incomplete and partial description of spatially varying data. It is of particular importance to discretize the domain under analysis into stochastic elements for representing random field, maintaining all the characteristic of the field described in the heterogeneous structure with adequate accuracy. This paper focuses on this issue by developing a stochastic computational strategy through combining a stochastic damage theory with isometric mapping (IsoMap) theory for model order reduction (MOR).

IsoMap theory was originally proposed by [16] for dimensionality reduction of nonlinear data sets. In this theory, every data element is connected to several other data elements using tree and graph concepts in a way to represent their inner nonlinear relationships. Therefore, this theory overcomes the shortcomings of traditionally dimensionality reduction techniques such as principal component analysis in preserving realistic features of realizations which are not arranged linearly in a sequential structure.

Principal component analysis theories use an orthogonal transformation to convert a set of observations of possibly correlated variables into a set of linearly uncorrelated variables called principal components regardless of original linear or nonlinear structure of correlated data points.

This paper is primarily concerned with predicting crack propagation in heterogeneous materials. Variational formulation proposed by [17] is implemented in the framework of a stochastic setting. A key component of the proposed framework is the introduction of an energy-based crack propagation direction criterion for randomly heterogeneous materials. The formulation provides both a rigorous theoretical method derived from Griffith's concept of energy restitution between bulk and surface energies, and numerical schemes capable of dealing with complex unknown crack paths. Energy release rate is defined as a function of the randomly variable fracture energy and elastic modulus, introducing randomness in the

stiffness matrix. This is particularly beneficial as these properties, which represent the resistance of the material to crack advancement and deformation, are considered to be significant factors in determining the fracture network patterns. Automatic mesh refinement is implemented to subdivide the elements at the area with a high probability of failure for the purpose of reducing computational time. IsoMap is employed as dimensionality reduction technique in order to reduce the computational cost added by sampling random values for material properties. It is used in combination with a mapping procedure based on the so called 'midpoint method', which assigns a random field value obtained at the location of the centroid of a certain random field element to the corresponding element in finite element mesh. Monte Carlo simulations of crack propagation are carried out in order to predict realistic and more tortuous crack patterns and to evaluate the structural reliability of the heterogeneous system. The resulting strategy proposes possible simplifications to describe realistic models of the topology and property variation and provides improvements in reliability and efficiency in computational algorithms of stochastic continuum damage theory.

2. Fracture advancement methodology

2.1. The variational approach

On the basis of the variational approach in fracture mechanics, developed by [18], the total energy of a brittle body in a reference configuration $\Omega \subset \mathbb{R}^N$ is defined as the sum of the bulk and surface energies

$$\mathcal{E}(\boldsymbol{f}, K) = \int_{\Omega \setminus K} W\big(\boldsymbol{F}(x)\big)dx + G\mathcal{H}^{N-1}(K) \tag{1}$$

where $\boldsymbol{f}$ is the body deformation, K is the fractured zone, $W: \mathbb{R}^{NxN} \rightarrow \mathbb{R}$ is the stored energy function, $\boldsymbol{F}$ is the deformation gradient, G is the fracture energy and $\mathcal{H}^{N-1}$ is the Hausdroff measure of K which provides the measure of the length of the crack for sufficiently regular fractured zone. The first and the second terms on the right hand side of the Equation 1 represent bulk and surface energy of the body, respectively.

Deformation of the elastic body under load increases the bulk energy. When this value reaches to a critical value in a given zone, it is energetically favourable for the system to release its energy. Therefore, crack growth is traced by consequent minimization of energy

function (i.e., Equation 1) at fixed time steps. The minimization of the Equation 1 with respect to any kinematically admissible displacement and any set of crack paths introduces a high level of complexity for the solution of the discontinuity problems, particularly due to the presence of the non-smooth values of the *K* parameter. Following the methodology proposed by [19], we introduce *K* as a set of discontinuity points S_f of the function $\boldsymbol{f}$, and set the problem in a space of discontinuous functions. The formulation of the energy, by replacing the term *K* with a set of jump points S_f of deformation in a Sobolev space $(\Omega; \mathbb{R}^N)$, is therefore given by

$$\mathcal{E}(\boldsymbol{f}) = \int_{\Omega \setminus K} W(\nabla \boldsymbol{f}) dx + G\mathcal{H}^{N-1}(S_f). \tag{2}$$

Presence of the term $\mathcal{H}^{N-1}(S_f)$ creates difficulties in finite element discretization of the function. To overcome such challenges, Equation 2 is approximated, in the sense of Γ-convergence [20], using a family of numerically more tractable functions defined over a Generalized Sobolev Space (GSBV). Based on the regularized formulation of the energy function for brittle fracture problems, [20 and 21], an auxiliary variable *s*, which is called damage parameter, is introduced. The parameter *s* is a regularized representation of the fractured zone defining the jump set in Equation 2. Therefore, a matric space *X* is considered which its elements are pairs of ($\boldsymbol{f}$, *s*). Then function $\mathcal{F} : X \rightarrow [0,+\infty]$ is used, which is defined as

$$\mathcal{F}(\boldsymbol{f}, s) = \begin{cases} \mathcal{E}(\boldsymbol{f}) & \text{if } \boldsymbol{f} \in \mathcal{D}, s \equiv 1 \\ +\infty & \text{otherwise} \end{cases} \tag{3}$$

where $\mathcal{D}$ is the domain of the functions belonging to GSBV. We consider the problem of minimizing $\{ \mathcal{F}(\boldsymbol{f}, s) : (\boldsymbol{f}, s) \in X \}$ to calculate the damage parameter. The damage parameter provides a picture of the damage state of the body, for an undamaged and intact body *s* is equal to 1 everywhere; while, it goes to zero in proximity of the jump set S_f.

Following [20], the functional formulation for a general $d > 1$ is expressed in the form provided in [21] as

$$\mathcal{F}_\varepsilon(\boldsymbol{f}, s) = \int_\Omega (s^2(x) + \kappa_\varepsilon) W\big(\boldsymbol{F}(x)\big) dx + G \int_{\Omega'} \left(\frac{\varepsilon^{\ell-1}}{\ell} |\nabla s(x)|^\ell + \frac{c}{\varepsilon \ell'} (1 - s(x))^\ell \right) dx \tag{4}$$

where ℓ is the ℓ^{th} power of the norm of the function defined in the Sobolev space, $\ell' = \ell / (\ell - 1)$, $c = \left(2 \int_0^1 (1-t)^{\ell/\ell'} dt\right)^{-\ell'}$ is the normalization constant, κ_ε is a positive regularization parameter and ε is related to the material length scale. Bulk and surface terms are two integrations over two different physical Ω and logical domain Ω'. Ω' is defined as an open set such that

$$\Omega \subset \Omega', \qquad \partial_2\Omega \subset \partial\Omega', \qquad \text{int}\, \partial_1\Omega \cap \partial\Omega' = \emptyset$$

where $\partial_1\Omega$ and $\partial_2\Omega$ are two disjoint parts of the boundary of Ω, and $\text{int}\, \partial_1\Omega$ is the interior of $\partial_1\Omega$ relative to $\partial\Omega$. The choice of the size of the logical domain is made on the consideration that it has to be big enough to avoid underestimation of the fracture energy when the crack reaches the boundary $\partial_1\Omega$.

For a two-dimensional problem where $\ell = 2$, the total energy formulation for the body can be represented as:

$$\mathcal{F}_\varepsilon(\boldsymbol{f}, s) = \int_{\Omega_0} (s^2 + \kappa_\varepsilon) W(\nabla_0 \boldsymbol{f}) dx_0 + \frac{G}{2} \int_{\Omega_0'} \left(\varepsilon |\nabla_0 s|^2 + \frac{1}{\varepsilon} (1-s)^2 \right) dx_0 \tag{5}$$

where Ω_0 and Ω_0' represent initial unfractured and stress-free configuration of the body in the physical and logical domains, respectively, x_0 represents a physical point of the physical domain Ω_0 and ∇_0represents the gradient with respect to x_0.

2.2. Stored Energy formulation

Following [17], we used an isotropic, compressible neo-Hookean type stored energy model that is defined as

$$W(\boldsymbol{F}) = \frac{\mu}{2}(\mathrm{tr}\boldsymbol{C} - 2) + \Psi(J) \tag{6}$$

where μ is the Lamé's second parameter, and $\boldsymbol{C}$ is the right Cauchy-Green tensor. In the above equation, the first term represents the classical formulation of an incompressible neo-Hookean material [22] and the second term is a convex function that is defined as [17]

$$\Psi(J) = \begin{cases} \frac{\lambda}{2}(\ln J)^2 - \mu \ln J & 0 \le J \le \jmath \\ \frac{\lambda}{2}(\ln J)^2 - \mu \ln J + (\lambda \ln J - \mu)\left(\frac{J - \jmath}{J}\right) & J \ge \jmath \end{cases}, \tag{7}$$

where μ is the Lamé's first parameter and $\jmath = e^{(\lambda+\mu)/\lambda}$. The Equation 7 is directly related to surface deformation, as it is function of the Jacobian of the deformation gradient (J). As J goes to zero the stored energy function goes to infinity, penalizing the extreme compression. To account for the tension-compression asymmetry of damage behavior of material, we followed the methodology proposed in [23], and the energy function is decomposed into two parts; a positive part which is considered to contribute to damage, and a negative part that resists to damage:

$$W(\boldsymbol{F}) = W^+ + W^- \tag{8}$$

where

$$W^+ = (s^2 + k_\varepsilon)\, W|_{J>1} \tag{9}$$

$$W^- = (1 + k_\varepsilon)\, W|_{J<1} \tag{10}$$

In the above equations, it can be noticed that the damage parameter appears only in the positive part of the energy function, the part associated to the elements that increase in surface (i.e., in the elements with $J > 1$), the value for damage in the elements is kept as calculated. The elements that decrease in surface (i.e., the elements with $J < 1$), do not contribute in damage. In this way, different behaviors for tension and compression are explicitly taken into account.

2.3. Numerical solution strategy

An approximation solution of minimization of the Equation 5 is achieved using an iterative procedure, shown in algorithm 1, which consists of imposing a stationary condition alternatively to one of the deformation and damage variables, while keeping the other variable fixed. For all $v \in W^{l,d}(\Omega, \mathbb{R}^n)$, $w \in W^{l,d}(\Omega_0)$, we look for a deformation that satisfy the stationary condition of

$$\delta\mathcal{F}_\varepsilon(\boldsymbol{f}_n, s_{n-1})[v, 0] = \int_{\Omega_0}(s_{n-1}^2(x_0) + k_\varepsilon)S\big(\nabla_0 \boldsymbol{f}_n(x_0)\big).\nabla_0 v(x_0)dx_0 = 0, \tag{11}$$

and then for the scalar field s stationary condition of

$$\delta\mathcal{F}_\varepsilon(\boldsymbol{f}_n, s_n)[0, w] = \int_{\Omega_0} 2W(\nabla_0 \boldsymbol{f}_n)s_n w\, dx_0 + G\int_{\Omega_0'} \varepsilon\nabla_0 s_n \cdot \nabla_0 w - \frac{(1-s_n)w}{\varepsilon}\, dx_0. \tag{12}$$

where $\boldsymbol{S}(\boldsymbol{F}) = \frac{\partial}{\partial \boldsymbol{F}} W(\boldsymbol{F})$ is the first Piola-Kirchhoff stress tensor.

By taking the Updated Lagrangian formulation of Equation 11 and linearization of that we obtain [17]

$$\begin{aligned}\int_{\Omega_{n-1}} (s_{n-1}^2 + k_\varepsilon)\Big((\det \boldsymbol{F})^{-1}(\boldsymbol{I} \boxtimes \boldsymbol{F})[\boldsymbol{S}(\boldsymbol{F})] \\ + (\det \boldsymbol{F})^{-1}(\boldsymbol{I} \boxtimes \boldsymbol{F})\frac{\partial S(\boldsymbol{F})}{\partial F}(\boldsymbol{I} \boxtimes \boldsymbol{F})^T[\nabla \bar{u}_n]\Big) \cdot \nabla v\, dx = 0\end{aligned} \tag{13}$$

where $\boxtimes$ represets the conjugation product [17] and using Equation 7

$$\mathbf{S}(\boldsymbol{F}) = \begin{cases} \mu\boldsymbol{F} + (\lambda ln J - \mu)\boldsymbol{F}^{-T} & 0 \le J \le j \\ \mu\boldsymbol{F} + \lambda e^{-(\lambda+\mu)/\lambda} J\boldsymbol{F}^{-T} & J \ge j \end{cases}. \tag{14}$$

Applying the integration by parts, we obtain the final weak form of Equation 12 as [17]

$$\int_{\Omega_0} 2W(\nabla_0 \boldsymbol{f}_n)s_n w\, dx_0 - G\int_{\Omega_0'}\left(\varepsilon\Delta_0 s_n - \frac{1-s_n}{\varepsilon}\right) w\, dx_0 = 0. \tag{15}$$

MATLAB Partial Differential Equation Toolbox together with the Newton-Raphson iteration scheme is used to solve the above equations. The iteration stops when two consecutive pairs of solution (f_{n-1}, s_{n-1}) and (f_n, s_n) are close enough according to an identified convergence condition. In order to avoid the healing of the cracks, an approximation method was used to consider irreversibility condition for damage evolution. We followed the methodology proposed by [17]. Based on that, irreversibility condition of $s_n(x) = s_{n-1}(x)$ if $s_n(x) > s_{n-1}(x)$ is set, and the value of damage parameter associated to each point in the body cannot exceed the one calculated at the previous time step. We leave the development of more advanced and rigorous methods for incorporating the irreversibility condition to future works.

Algorithm 1: Numerical solution procedure

Model input: Identifying model parameters, problem geometry and boundary conditions and initialization: Set $(\boldsymbol{f_n^0}, \boldsymbol{s_n^0}) = (\boldsymbol{f_{n-1}}, \boldsymbol{s_{n-1}})$

while $\left\| \boldsymbol{s_n^j} - \boldsymbol{s_n^{j-1}} \right\|_{L^\infty(\Omega_0)} > \boldsymbol{s_{max}}$

  for *a given* $(\boldsymbol{f_n^{j-1}}, \boldsymbol{s_n^{j-1}})$

  compute an approximate solution $\boldsymbol{f_n^j}$ for fixed $\boldsymbol{s}$

  compute $\boldsymbol{s_n^j}$ for fixed $\boldsymbol{f}$

end

Irreversibility condition: Set $\boldsymbol{s_n^j(x_0) = s_n^0(x_0)}$ at all nodal points at which $\boldsymbol{s_n^0(x_0)}$ becomes smaller than a given $\boldsymbol{\check{s} > 0}$.

We also used an adaptive h refinement strategy [17] to automatically refine the elements with values of s lower that given thresholds. At new nodes generated through the remeshing strategy, values of displacement and damage are calculated by linear interpolation from the existing nodes.

3. Stochastic approach

For modeling material heterogeneity, simulations with both one and two random variables are executed. The Weibull distribution function [24] is used to generate samples of the fields, as it has a simple structure and its applicability for modelling failure of brittle materials has been tested [25-28]. For the simulation with only one random field, Cumulative Density Function (CDF), denoted by P(.), and Probability Density Function (PDF), denoted by p(.), for Weibull distribution, which are plotted in Figure 1, take the form of

$$P(\sigma) = 1 - exp\left(-\left(\frac{\sigma}{\sigma_0}\right)^m\right) \tag{16}$$

$$p_s(\sigma) = \frac{dP(\sigma)}{d\sigma} = \frac{m}{\sigma_0}\left(\frac{\sigma}{\sigma_0}\right)^{m-1} exp\left(-\left(\frac{\sigma}{\sigma_0}\right)^{m}\right) \tag{17}$$

where σ is the random parameter, m is the shape parameter and σ_0 is the scale parameter.

Maximum Likelihood Estimator (MLE) is used to define both the shape and the scale parameters. Let $\sigma_1, \sigma_2, \ldots.\sigma_n$ be a set of hypothetical data which is randomly generated. It is plausible to fit a Weibull distribution to this hypothetical data [25-28]. In other words, we assume that $\sigma_1, \sigma_2, \ldots.\sigma_n$ constitute a sample of size n taken from a Weibull distribution with the PDF given in (17) where the $p_{\sigma_i}(\sigma_i, m, \sigma_0)$ σ_0 and m are unknown parameters. These parameters can be estimated using the Maximum Likelihood (ML) method. For the hypothetical sample $\sigma_1, \sigma_2, \ldots. \sigma_n$ taken from $p_{\sigma_i}(\sigma|m, \sigma_0), \sigma_0$ the likelihood function $L(\sigma_0, m, \sigma_1, \ldots \sigma_n)$ which is the joint density function of the n random variables defined as

$$L(\sigma_0, m, \sigma_1, \ldots \sigma_n) = p(\sigma_1, \sigma_2, \ldots \sigma_n|\sigma_0, m) = \prod_{i=1}^{n} p_{x_i}(\sigma_i|\sigma_0, m) \tag{18}$$

The maximum likelihood estimations (MLEs) of (σ_0, m) are derived by maximising the likelihood function L given in (18) with respect to (σ_0, m). This can be done by simultaneously solve the following equations:

$$\frac{dLog(L)}{dm} = 0., \qquad \frac{dLog(L)}{d\sigma_0} = 0. \tag{19}$$

In order to obtain the MLEs of the Weibull parameters, we first substitute Equation (17) into Equation (18) and then solve Equation (19) to achieve the following system of equations [28]:

$$\frac{\sum_{i=1}^{n} \ln(\sigma_i){\sigma_i}^m}{\sum_{i=1}^{n} {\sigma_i}^m} - \frac{1}{n}\sum_{i=1}^{n} \ln(\sigma_i) - \frac{1}{m} = 0 \tag{20a}$$

$$\sigma_0 = \left(\frac{\sum_{i=1}^{n} {\sigma_i}^m}{n}\right) \tag{20b}$$

Unfortunately, this system of equations cannot be analytically evaluated and an iterative numerical algorithm should be used to solve it. We first apply Newton-Raphson algorithm on Equation (20a) to present m in terms of σ_0, the details of Newton-Raphson algorithm to obtain the estimation of m are as follows:

$$m_{n+1} = m_n - \frac{f(m_n)}{f'(m_n)} \tag{21}$$

where

$$f(m_n) = \sum_{i=1}^{n} \sigma_i^m \ln(\sigma_i) \Big/ \sum_{i=1}^{n} \sigma_i{}^m - \frac{1}{m} - \frac{1}{n}\sum_{i=1}^{n} \ln(\sigma_i) \tag{22}$$

and

$$f'(m_n) = \sum_{i=1}^{n} \sigma_i^m (\ln \sigma_i)^2 - \frac{1}{m^2}\sum_{i=1}^{n} \sigma_i^m (\mathrm{m} \ln(\sigma_i) - 1) - \left(\frac{1}{n}\sum_{i=1}^{n} \ln(\sigma_i)\right)\left(\frac{1}{n}\sum_{i=1}^{n} \sigma_i^m \ln(\sigma_i)\right). \tag{23}$$

The estimated value of m, denoted by $\hat{m}$, is then substituted into Equation (20b) to obtain the estimation of scale parameter σ_0 denoted by $\hat{\sigma}_0$ and finally define the Weibull distribution function. Given the estimated parameters, $(\hat{m}, \hat{\sigma}_0)$ we can generate random realisations from the Weibull distribution over the simulation domain using the inverse method [29]. In this method, we first draw a sample $u_1, \dots, u_n$ from a uniform distribution defined over (0,1), and the corresponding sample taken from Weibull distribution can be then obtained by solving the following equation

$$\sigma_i = P^{-1}(u_i) = -\hat{\sigma}_0 \sqrt[\hat{m}]{\ln(1-u_i)}, \qquad for\ i = 1, \dots, n \tag{24}$$

In this work, the Young's modulus and fracture energy are represented by two dimensional correlated stochastic fields. For the generation of a bivariate random field, the use of a multivariate Weibull PDF and CDF is needed. The approach used in this work, known as Normal-to-anything (NORTA), is to obtain the multivariate Weibull PDF from the multivariate Standard Normal PDF applying the change of variable. The details of formulation of the bivariate Weibull distribution considered in this work is the one proposed

in [30] and the transformation function between Gaussian to any other non-Gaussian distribution is also explicitly expressed in [31]. We briefly present this methodology to generate samples from the bivariate Weibull distribution derived from its relationship to the bivariate standard normal distribution. The bivariate standard normal PDF is given by

$$f(x_{1N}, x_{2N}|\rho) = \frac{1}{2\pi\sqrt{1-\rho^2}} \exp\left(-\frac{1}{2(1-\rho^2)}(x_{1N}^2 + x_{2N}^2 - 2\rho x_{1N} x_{2N})\right) \quad (25)$$

where ρ is the correlation coefficient between hypothetical random variables generated by the normal distributions [30] and is calculated by the exponential correlation function proposed in [26].

The bivariate Weibull distribution can be then obtained from the following equation

$$p_w(\sigma_{1W}, \sigma_{2W}|\sigma_{01}, \sigma_{02}, m_1, m_2, \rho) = f(x_{1N}, x_{2N}|\rho) \left| \begin{matrix} \frac{\partial \sigma_{1W}}{\partial x_{1N}} & \frac{\partial \sigma_{1W}}{\partial x_{2N}} \\ \frac{\partial \sigma_{2W}}{\partial x_{1N}} & \frac{\partial \sigma_{2W}}{\partial x_{2N}} \end{matrix} \right|^{-1} \quad (26)$$

By substituting Equation (25) into Equation (26), the bivariate Weibull distribution depending on five parameters (including 2 shape parameters, 2 scale parameters and the correlation coefficient parameter, ρ) takes the following form

$$p_W(\sigma_{1W}, \sigma_{2W}|\sigma_{01}, \sigma_{02}, m_1, m_2, \rho) =$$

$$= \frac{1}{4\sqrt{1-\rho^2}} \frac{e^{\left(-\frac{1}{2(1-\rho^2)}(x_{1N}^2 + x_{2N}^2 - 2\rho x_{1N} x_{2N})\right)}}{\left| \prod_{i=1}^{2} \frac{\sigma_{0i}}{m_i} \frac{e^{\left(-\frac{x_{iN}^2}{2}\right)}}{\left(1 - \mathrm{erf}\left(\frac{x_{iN}}{\sqrt{2}}\right)\right)} \left(-\log\left(\frac{\left(1 - \mathrm{erf}\left(\frac{x_{iN}}{\sqrt{2}}\right)\right)}{2} \right) \right)^{m_i^{-1}-1} \right|}. \quad (27)$$

Equation (27) can be then fully represented in terms of $(\sigma_{1W}, \sigma_{2W})$ using the relationship between normally-distributed variables and the Weibull distributed ones as expressed in [30, 31] and given below

$$x_{iN} = \sqrt{2}\,\mathrm{erf}^{-1}\left(1 - 2\,e^{\left(-\left(\frac{\sigma_{iW}}{\sigma_{0i}}\right)^{m_i}\right)}\right) \tag{28}$$

The inverse of (28), represented in (29) can be used to generate samples from bivariate Weibull distribution in terms of the samples taken from the bivariate standard normal distribution:

$$x_{iW} = \sigma_{0i}\left[-\log\left(\frac{1 - \mathrm{erf}\left(\frac{x_{iN}}{\sqrt{2}}\right)}{2}\right)\right]^{\frac{1}{m_i}} \tag{29}$$

The algorithm for generating realizations from a bivariate Weibull-distributed random field is expressed as follows:

1) Generate a hypothetical data according to probabilistic characteristics of the heterogeneous material
2) Given the hypothetical data, the parameters of the bivariate Weibull distribution are estimated using ML method, denoted by $(\hat{m}_1, \hat{m}_2, \hat{\sigma}_{01}, \hat{\sigma}_{02}, \hat{\rho})$.
3) A sample of desired size can be easily drawn from a bivariate standard normal distribution with the estimated correlation coefficient, $\hat{\rho}$. We illustrate this bivariate sample as $\left\{\left(x_{1N}^{(i)}, x_{2N}^{(i)}\right), i = 1,2,\ldots,n\right\}$
4) By replacing the sample generated in Step 3 into Equation (27), a bivariate sample $\left\{\left(x_{1W}^{(i)}, x_{2W}^{(i)}\right), i = 1,2,\ldots,n\right\}$ can be generated from the bivariate Weibull distribution with the estimated parameters $\hat{m}_1, \hat{m}_2, \hat{\sigma}_{01}, \hat{\sigma}_{02}, \hat{\rho}$.

The size of the elements for stochastic discretisation should be selected to adequately capture the essential features of the stochastic spatially variable properties during the sampling phase. It should not be too large to cause underestimation of the spatial variability and should not be too small to prevent the numerical instability problems related to the decomposition of a too large covariance matrix [32]. Relationships for the optimal ratio between mesh size and correlation length of random properties as a measure of heterogeneity are provided in several studies [26 and 28]. It is suggested that the size of the element should be less than the half of the correlation length, and for optimal results, the element size of the mesh should be between one quarter and one half of the correlation length. For this study a *dual mesh*

methodology is employed, and therefore two different meshes are identified: a stochastic mesh, containing all the information related to the material heterogeneity, and a finite element mesh for the fracture problem. The material length scale defines the size of the initial stochastic mesh. IsoMap technique is used to reduce the dimensionality of the stochastic mesh. This simplifies and accelerates materials stochastic analysis tasks through constructing isometric low-dimensional representation of material formation variations.

4. Model Order Reduction (MOR)

4.1. IsoMap

Each realization with D elements is considered as a point in D-dimensional space. Our plan is to map each realization to a d-dimensional space ($d << D$) while the intrinsic characteristics in the realization will be well maintained. We compute all the geodesic distances between all pairs of data points. The geodesic distance can be understood to be the shortest distance between the sample points in the high-dimensional space and is computed by constructing a neighbourhood graph $\mathcal{G}$ in which every point is connected with its k nearest neighbours $\sigma_{ij}(j = 1, 2, \ldots, k)$. After choosing the size of the neighbourhood, we calculate the distances between all pairs of elements (distances are calculated between elements barycentre) and define the distance between elements as d_E(i,j). Then, a line between each two neighbouring points is drawn if their distance is included within the neighbourhood size. By repeating this process for all the elements we will obtain the neighbourhood graph. The shortest pattern between points is calculated. The shortest path between two points in the graph forms an estimate of the geodesic distance between these two points, and can be computed by means of Floyd's algorithm [32].

Geodesic distance d_M between two points for IsoMap is measured by summing all the distances between points within the two nodes under consideration. The distances between points are initialised to $d_M = d_E$ if two points are directly connected and, to $d_M = \infty$ otherwise. For each couple of points, the shortest path is then defined as

$$d_M(i,j) = min\{d_M(i,j), d_M(i,k) + d_M(k,j)\} \tag{30}$$

and is known as Floyd's algorithm [32].

The matrix of shortest path distances is defined as $(D_M)_{ij} = (d_M(i,j))^2$. In the next step, we calculate the matrix

$$\mathfrak{C}(D_M) = -\boldsymbol{H}\boldsymbol{D}_{\boldsymbol{M}}\boldsymbol{H}/\mathbf{2} \tag{31}$$

where $\boldsymbol{H}$ is the "centering matrix" defined by [16] as $H_{ij} = (\delta_{ij} - 1/D)$, with δ_{ij} being the Kronecker delta. The eigenvalues λ_d of the matrix $\mathfrak{C}(D_M)$ are calculated and sorted in decreasing order. The new dimension d is specified by estimating the cumulative residual variance, defined as a measure of the difference between the initial and the reduced spatial configuration, given by the eigenvalues λ_d. The new dimension d is defined as the dimension for which the convergence criteria for cumulative variance is reached. Figure 2 shows the procedure followed for getting the reduced order stochastic model.

The new dimension d is directly connected to the size of its neighbourhood. Table 1 summarizes how d changes for a change of k for a sample of stochastic realization on a circular domain.

In terms of computational effort, in Figure 3 we can observe how the time needed for generating a sample is decreasing when the size of the stochastic mesh increases until it reaches its optimal dimension.

Based on the above, and considering the required precision level and its necessary computational effort, the values of k equal to 9 and d equal to 307 are selected, as this combination reduces the computational cost of the sampling phase.

4.2. Mapping from random field to finite element mesh

After generating the reduced order mesh, we select a mapping procedure for transferring values of random parameter from the stochastic mesh to the finite element mesh.

This mapping is necessary, in order to maintain the same distribution of material properties over the physical domain.

The mapping is based on a graphical method which refers to the distance between elements and based on the 'midpoint method'. Each element of the finer mesh has a different value of fracture energy. The elements from the coarser mesh are projected, as shown in Figure 4, on those of the finer mesh. To assign a value of fracture energy the mapping employed here considers the values of fracture energy of those elements of the fine mesh in proximity of the single element of the coarse mesh. This procedure can be attributed to the spatial averaging

method, which assigns a value obtained as an average of stochastic field values over another finite element domain [33]. Essentially, for mapping the values of fracture energy between the two meshes, both values of fracture energy and distance between elements barycentre, representing the distance between the elements, are considered. The final value of fracture energy is assigned using Equation 32:

$$G_{FE} = \sum_{i=1}^{nr} \frac{G_{nr}}{d_{nr}} \tag{32}$$

where *nr* represents the number of element for which the relative distance between the reduced and the original barycentre is less than a given threshold which, for this work, is considered to be the size of the new mesh. In fact, as shown in Figure 4, the higher the distance between the elements is, the lower will be the influence of that element to the calculation of random parameter for the new element.

If during the analysis an element is refined, the new value of fracture energy will be assigned considering the same procedure in order to keep the same local heterogeneity distribution during the whole analysis.

The final equation describing the whole energy of the system, obtained by substituting Equation 32 into Equation 1, takes therefore the form

$$\mathcal{E}(f) = \int_{\Omega \setminus K} W(\nabla f) dx + \sum_{i=1}^{nr} \frac{G_{nr}}{d_{nr}} \mathcal{H}^{N-1}(S_f). \tag{33}$$

5. Numerical example

5.1. Brazilian test on a rock sample

The first example analysed is a cylindrical natural rock disc. The geometry, boundary and loading conditions of the sample are shown in Figure 5a. The thickness and radius of the sample are 36.58 mm and 18.76 mm, respectively. The sample is discretised using triangular elements. The finite element mesh with size 2 mm consists of 1189 triangular elements and 551 nodes that is shown in Figure 5b. Initially, the same mesh is used for the finite element and stochastic discretization.

Thickness of the damage zone and morphology of cracks are significantly influenced by the value of the ε. A better approximation for crack patterns would be achieved with the smaller value of the epsilon. However, this would lead to a smaller mesh size and high computational costs [34 and 35]. We followed Lancioni and Royer-Carfagni [36] and Bazant and Planas [37], for identifying the value of the ε. Based on the experimental observations, the value of epsilon is directly related to the size of the constituent grains of the material and should be approximately 2 to 3 times the size of constituent grains, and for this case-study we selected it to be equal to 2. In this study, a displacement-controlled condition was implemented. In [38], the authors mentioned that based on the International Society of Rock Mechanics's guidelines, the experimental set up for a Brazilian test is usually designed with a 5º to 15º contact arc between specimen and loading jaws, and accordingly in order to reproduce a realistic simulation, the length of the section where load is applied should be between 1.5 and 3.2 mm. Therefore, we applied a distributed displacement with a rate of 0.0005 mm/step over length equal to 2 mm at above and below of the disc. The residual stiffness k_ε is set equal to 0.01, to be one order of magnitude smaller than the finite element mesh size after refinement. Fracture energy is initially selected to be that property, with mean value of 2.5 x 10^{-2} N/mm and standard deviation equal to 0.1 x 10^{-3}, 0.5 x 10^{-3} and 1 x 10^{-3}. This value for fracture energy has been calculated from experiments following basic principles of fracture mechanics, given the geometry, the loading conditions and the modulus of elasticity. The three different standard deviations have been selected in order to study the effect of the degree of heterogeneity on the material response.

Spatial variation of the random parameter is described by the Weibull distribution, which is generated using Equation 24. Figure 6 shows a realization of this property, which is randomly distributed over the spatial domain. The crack path obtained for a model with this specific realization of the fracture energy is shown in Figure 7 and is compared with the crack path obtained from the homogeneous model. It is observed that crack path obtained from the model considering a heterogeneous material property shows a more tortuous pattern, as crack tends to propagate towards zones of less resistance.

Figure 8 shows a quick comparison explaining the importance of calculating a suitable reduced order model. In fact, with a reduced-order stochastic mesh we obtain a crack path almost identical to the one obtained with the initial stochastic mesh, which is not the case if we use a too coarse stochastic mesh.

In Figure 9 we can observe the evolution of the damage state of the body for both homogeneous and heterogeneous models. It shows that heterogeneity causes a random distribution of local damage zones in the domain, which significantly affects the mechanical performance of the body. Especially during the last steps of the simulation, it is clear how heterogeneity creates zones of weakness (low values of s) that will introduce that tortuous patterns observed in the crack path. These zones of weakness are not visible for the homogeneous model, where damage is concentrated only in correspondence of the loading points.

Stochastic response of the fracturing sample is computed using MC simulations. In Figures 10 and 11, the mean value and standard deviation of the tensile strength are plotted as a function of the number of MC simulations, which show that the statistical convergence is achieved after only 65 simulations.

In Figure 12 all the stress-strain curves resulted from MC simulations associated to different random realizations of fracture energy together with their mean curve are plotted. The tensile strength is considered as the maximum value of stress, which occur at the center of the disc, obtained through experiment and numerical simulations. It is calculated using the second Piola-Kirchoff stress tensor formulation defined as

$$\mathcal{P} = \mu \boldsymbol{I} + (\lambda \log J - \mu)\boldsymbol{C}^{-T}, \tag{34}$$

and accordingly the strains are considered at the centre of the disc defined as function of Lagrangian strain tensor.

Figure 13 compares stress-strain curves obtained from experimental test and numerical modelling considering simulations with both homogeneous and heterogeneous models. It is noticeable that the maximum tensile strength calculated from the stochastic based modelling is not very different from the one calculated by the homogeneous based modelling. The stochastic based modelling result shows a notably better agreement with experimental measurements particularly in terms of failure strain. The physical interpretation of the difference between strains at failure is related to the increase of material ductility for heterogeneous models, due to the higher roughness and tortuousness of cracks compared to those obtained with the homogeneous model.

Furthermore, we can observe how the local damages described above lead to a piecewise linear behaviour, in which material stiffness progressively decreases before failure, which still has brittle nature. The homogeneous model is not capable of reproducing this aspect of the sample behavior until brittle failure occurs.

Figure 14 shows the stress-strain curve for the three degrees of standard deviation considered in this study. Despite the different values of standard deviation, we can observe, especially for the first phases of the simulations, that the simulated behaviours are very close and differ only in the last phase, closer to failure. A higher standard deviation, i.e., index of a higher degree of heterogeneity, leads to a curve closer to the experimental plot compared to the results obtained from simulations with smaller values of standard deviation.

In order to study the effect of correlation between random parameters on the behaviour of fracturing body, we select both fracture energy and modulus of elasticity as random variables. A mean value of 29.1 GPa and standard deviation of 0.5 was selected for the modulus of elasticity. Three different degrees of correlation are analysed, for correlation coefficient equal to 1, 0.5 and 0, representing full, partial and absence of correlation, respectively.

Figure 15 shows the stress – strain curve for the three different scenarios and the mean curve obtained from the 100 Monte Carlo simulations. Figure 16 compares the three mean curves with the curve obtained experimentally and from the homogeneous model, from where we can observe that a full correlation moves the curve from the experimental plot, while a lower degree of correlation leads to more realistic results in terms of material strength. Figure 17 shows how convergence of the results is achieved after 60 analyses.

5.2. Case study 2: dog bone concrete specimen

The second example included in this study is the dog bone shaped concrete specimen studied experimentally by [39]. The specimen geometry and finite element discretization are shown in Figure 18. Mesh size is chosen equal to 7.5 mm, and therefore 117 nodes and 194 triangular elements are used to discretize the problem domain. The thickness of the specimen is 100 mm. Therefore, the problem is analysed under plane strain conditions, as the thickness (z-direction) of the problem is predominant on the other two directions. Dual mesh technique is employed also for this case study.

A value of 0.4 was selected for the epsilon in this case-study. The mean value for fracture energy, selected from literature [39], is equal to 0.95 x 10^{-1} N/mm, and four different values for the standard deviation, including $0.1x10^{-2}$, $0.5x10^{-2}$, $1x10^{-2}$ and $5x10^{-2}$, are considered.

The spatial fluctuation of the random parameter is described by Weibull distribution. Three different values of correlation length (l_c = 1.2, 15 and 30 mm) are used, corresponding to stochastic field of low, moderate and strong spatial autocorrelation. In order to guarantee mesh convergence, the mesh refinement procedure for those elements subjected to high damage is incorporated for this example as well. The ratio between the correlation length of the random field and ε is kept in the range suggested by previous contributions [26 and 28]. The size of the refined finite element mesh is between one half and one quarter of the minimum correlation length selected for discretizing the random fields.

Sample functions of a Weibull distributed stochastic field for standard deviation $5x10^{-2}$ and l_c equal to 1.2 and 15 mm are shown in Figure 19. It is clear how a higher degree of heterogeneity is given not only by a higher standard deviation in input, but also by a lower correlation length, as observed in the study of [40]. Figure 20 shows the crack patterns obtained for four realizations with two different degrees of standard deviation ($0.1x10^{-2}$ and $5x10^{-2}$) and two different correlation lengths (1.2 and 15 mm). It is worth noticing that in the case with higher spatial variability the crack paths show an extremely tortuous pattern compared to the others. Together with the final crack patterns, in Figure 21 also contour plots for damage parameter for different realizations are shown for the time step immediately before the failure.

The response variability is computed using MC simulation with sample size equal to 100. The statistical convergence achieved within this number for simulations with l_c = 1.2 mm and the standard deviation equal to $5x10^{-2}$, is shown in Figure 22.

Mean load-displacement curves obtained from the MC method corresponding to four different combined values of correlation length (l_c = 1.2 and 15 mm) and standard deviation ($0.1x10^{-2}$ and $5x10^{-2}$) are plotted in Figure 23. Comparison of the results shows that the low values of both standard deviation and correlation length are not capable to show a significant variation in the response of the material. Furthermore, if only one of the parameters is

modified to consider a higher degree of heterogeneity, the effect on the response is not appreciable. However, for low values of correlation length and high standard deviation a different mean curve is obtained, especially regarding the value of ultimate deformation on the elastic range. Figure 24 shows different plots for the same value of correlation length (l_c = 1.2 mm) and the four different values of standard deviation. Again, differences in the responses of different realizations are appreciable only for high standard deviations despite the low correlation length.

Figure 25 shows realization for the same simulation of both fracture energy and modulus of elasticity when different degrees of cross correlation between variables are considered (0.95, 0.5 and 0). The amount of variation for the fracture energy and modulus of elasticity is the same for the case with full correlation, while they vary randomly when cross correlation is equal to zero. Crack patterns are shown in Figure 26 together with the mesh topology after refinement.

The statistical convergence achieved within 100 MC simulations is illustrated for the three different values of cross correlation in Figure 27 where the mean value and standard deviation of the peak load are plotted. Convergence is achieved quicker when partial correlation between variables is considered.

Figure 28 shows the load–deformation curves obtained for different simulations with variable fracture energy and modulus of elasticity. Comparison with experimental results is provided. Always for an intermediate value of cross correlation the results are slightly closer to the experimental measurements. This conclusion is consistent with the results obtained by [41].

6. Conclusions

In this paper, we presented a new methodology for numerical modelling of crack propagation of heterogeneous materials. Ignoring heterogeneity of materials results in prediction of the crack paths, which are different from the experimental observations. This is mainly because of the local effects (such as defects and loading conditions) that are not considered in the homogeneous models. An appreciable difference can be noted in terms of material strength. The homogeneous models overestimate the value of material strength and provide a fully linear plot, and are not capable of accounting for nonlinearities and reduction in stiffness

induced by local heterogeneities. Such non-linearity is visible also in the experimental plots. By incorporating the effect of heterogeneity, the numerical stress-strain plots coming from MC simulation method become closer to the experimental observations, in terms of both material strength and curve trends.

By introducing the effect of heterogeneity, crack patterns don't change significantly, as they are mostly determined by loading configuration and boundary conditions. They keep their major trends while becoming more tortuous.

If multiple random variables are considered, results show that a high correlation leads to less realistic results compared to lower values of correlation. The application of a nonlinear dimensionality reduction technique leads to similar results, with the advantage in reducing the CPU time, especially the time associated to the sampling phase.

Acknowledgment

This study was supported by EPSRC UK (No. EP/M506679/1). We thank Dr Giovanni Lancioni in Marche Polytechnic University, Italy for helpful discussions on continuum damage theory and providing the computer program subroutines used for finite element mesh refinements.

References

1. Geers, M. G. D., Kouznetsova, V. G., & Brekelmans, W. A. M. Multi-scale computational homogenization: Trends and challenges. *Journal of computational and applied mathematics* 2010; *234*(7): 2175-2182.
2. Miehe, C., & Bayreuther, C. G. On multiscale FE analyses of heterogeneous structures: from homogenization to multigrid solvers. *International Journal for Numerical Methods in Engineering* 2007; *71*(10): 1135-1180.
3. Mousavi Nezhad, M., Javadi, A. A., & Abbasi, F. Stochastic finite element modelling of water flow in variably saturated heterogeneous soils. *International Journal for Numerical and Analytical Methods in Geomechanics* 2011; *35*(12): 1389-1408.
4. Gutierrez M. and de Borst, R. Deterministic and stochastic analysis of size effects and damage evolution in quasi-brittle materials. *Archive of Applied Mechanics* 1999; 69: 655-676.
5. Bažant, Z.P., Pang, S., Vořechovský, M. and Novák, D. Energetic–statistical size effect simulated by SFEM with stratified sampling and crack band model. *International Journal for Numerical Methods in Engineering* 2007; 71(11): 1297–1320.

6. Nouy, A. and Clément, A. eXtended Stochastic Finite Element Method for the numerical simulation of heterogeneous materials with random material interfaces. *International Journal for Numerical Methods in Engineering* 2010; 83(10): 1312–1344.
7. Saouma, V. E., and Ingraffea, A. R. Fracture mechanics analysis of discrete cracking. In *Proceedings of IABSE Colloquium on Advanced Mechanics of Reinforced Concrete, Delft, the Netherlands* 1981; 413-436.
8. Rashid, Y. R. Ultimate strength analysis of prestressed concrete pressure vessels. *Nuclear engineering and design* 1968; *7*(4): 334-344.
9. Rena, C. Y., Ruiz, G., & Chaves, E. W. A comparative study between discrete and continuum models to simulate concrete fracture. *Engineering Fracture Mechanics* 2008; *75*(1): 117-127.
10. Tomar, V., & Zhou, M. Deterministic and stochastic analyses of fracture processes in a brittle microstructure system. *Engineering fracture mechanics* 2005; *72*(12): 1920-1941.
11. Espinosa, H. D., & Zavattieri, P. D. A grain level model for the study of failure initiation and evolution in polycrystalline brittle materials. Part I: Theory and numerical implementation. *Mechanics of Materials* 2003; *35*(3): 333-364.
12. Zhou, F., & Molinari, J. F. Stochastic fracture of ceramics under dynamic tensile loading. *International journal of solids and structures* 2004; *41*(22): 6573-6596.
13. Kaczmarczyk, L., Mousavi Nezhad, M., and Pearce, C. Three-dimensional brittle fracture: configurational-force-driven crack propagation. *International Journal for Numerical Methods in Engineering* 2014; 97(7): 531-550.
14. Bažant, Z. P., & Pijaudier-Cabot, G. Measurement of characteristic length of nonlocal continuum. *Journal of Engineering Mechanics*, ASCE 1989; 115 (4): 755-767.
15. Mahadevan, S. and Haldar, A. Practical random field discretization in stochastic finite element analysis. Struct. Safety 1991; 9: 283-304.
16. Tenenbaum, J. B., De Silva, V., & Langford, J. C. A global geometric framework for nonlinear dimensionality reduction. *Science* 2000; *290* (5500): 2319-2323.
17. Del Piero, G., Lancioni, G., & March, R. A variational model for fracture mechanics: numerical experiments. *Journal of the Mechanics and Physics of Solids* 2007; *55*(12): 2513-2537.
18. Francfort, G. A., & Marigo, J. J. Revisiting brittle fracture as an energy minimization problem. *Journal of the Mechanics and Physics of Solids* 1998; *46*(8): 1319-1342.
19. Ambrosio, L., Tortorelli, V.M. Approximation of functionals depending on jumps by elliptic functionals via G-convergence. Commun. Pure Appl. Math. 1990; 43: 999–1036.
20. Bourdin, B., Francfort, G. A., & Marigo, J. J. Numerical experiments in revisited brittle fracture. *Journal of the Mechanics and Physics of Solids* 2000; *48*(4): 797-826.
21. Ambrosio, L., & Braides, A. Energies in SBV and variational models in fracture mechanics. In: Cioranescu, D., et al. (Eds.), Homogenization and Applications to Material Sciences, GAKUTO International Series Mathematical Sciences and Applications, 1995; 9: 1–22.
22. Bonet, J. and Wood, R.D. Nonlinear continuum mechanics for finite element analysis, Cambridge University Press, 1997.

23. Li, T., Marigo, J.J., Guilbaud, D. and Potapov, S. Gradient damage modeling of brittle fracture in an explicit dynamics context. International Journal for Numerical Methods in Engineering 2016; 108(11):1381-405.
24. Weibull, W. *The phenomenon of rupture in solids*. Generalstabens Litografiska Anst. 1939.
25. Fang, Z., & Harrison, J. P. Development of a local degradation approach to the modelling of brittle fracture in heterogeneous rocks. *International Journal of Rock Mechanics and Mining Sciences* 2002; *39*(4): 443-457.
26. Yang, Z., & Frank Xu, X. A heterogeneous cohesive model for quasi-brittle materials considering spatially varying random fracture properties. *Computer methods in applied mechanics and engineering* 2008; *197*(45): 4027-4039.
27. Gorjan, L., & Ambrožič, M. Bend strength of alumina ceramics: A comparison of Weibull statistics with other statistics based on very large experimental data set. *Journal of the European Ceramic Society* 2012; *32*(6): 1221-1227.
28. Vu, K. A. and Stewart, M. G. Predicting the likelihood and extent of reinforced concrete corrosion-induced cracking. *Journal of structural engineering* 2005; *131*(11): 1681-1689.
29. Devroye, L. Non-Uniform Random Variate Generation. Springer, 1986
30. Villanueva, D., Feijóo, A. and Pazos, J.L. Multivariate Weibull distribution for wind speed and wind power behavior assessment. Resources. 2013;2(3):370-84.
31. Faraz, A., Saniga, E.M. and Heuchenne, C. Shewhart control charts for monitoring reliability with Weibull lifetimes. Quality and Reliability Engineering International. 2015;31(8):1565-74.
32. Floyd, R. W. Algorithm 97: shortest path. *Communications of the ACM* 1962; *5*(6): 345.
33. Haldar, A., & Mahadevan, S. Probability, reliability, and statistical methods in engineering design 2000; 1: New York: Wiley.
34. Amor, H., Marigo, J. J., & Maurini, C. Regularized formulation of the variational brittle fracture with unilateral contact: Numerical experiments. *Journal of the Mechanics and Physics of Solids*, 2009; *57*(8): 1209-1229.
35. Bourdin, B., Marigo, J. J., Maurini, C. and Sicsic, P. Morphogenesis and propagation of complex cracks induced by thermal shocks. Physical Review Letters 2014; 112:014301.
36. Lancioni, G. and Royer-Carfagni, G. The Variational Approach to Fracture Mechanics. A Practical Application to the French Panthéon in Paris. Journal of Elasticity 2009; 95: 1–30.
37. Bazant, Z. P., & Planas, J. Fracture and size effect in concrete and other quasi-brittle materials. 1997, CRC press.
38. Li, D. and Wong, L.N.Y. The Brazilian disc test for rock mechanics applications: review and new insights. Rock mechanics and rock engineering 2013; *46*(2): 269-287.
39. van Vliet, M. R. A. Size effect in tensile fracture of concrete and rock. TU Delft, Delft University of Technology 2000.
40. Georgioudakis, M., Stefanou, G., & Papadrakakis, M. Stochastic failure analysis of structures with softening materials. *Engineering Structures* 2014; 61: 13-21.
41. Carmeliet, J., & Hens, H. Probabilistic nonlocal damage model for continua with random field properties. *Journal of engineering mechanics* 1994; 120(10): 2013-2027.

Tables

Table 1. Dimension and mesh size for optimal cumulative variance trend for different sizes of neighbourhood *k*

	Cumulative Variance 0.95		Cumulative Variance 0.9	
k	***d***	**Mesh size (mm)**	***d***	**Mesh size (mm)**
3	71	5.7	65	6.1
4	103	4.6	94	4.8
5	140	3.9	127	4
6	180	3.3	164	3.5
7	246	2.8	223	2.9
8	290	2.6	264	2.75
9	307	2.5	279	2.7
10	342	2.4	310	2.5
11	375	2.3	341	2.35
12	424	2.25	383	2.3
13	460	2.2	412	2.25
14	488	2.2	432	2.25
15	551	2	473	2.2
16	551	2	508	2.1
17	551	2	551	2

Figures

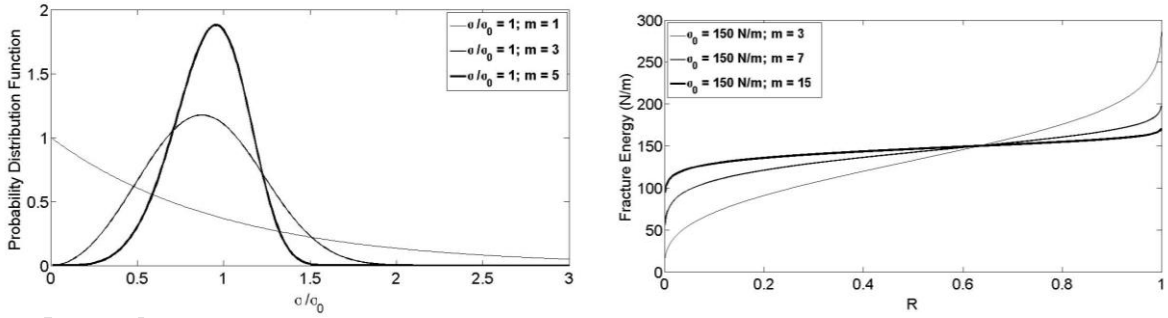

Figure 1. Weibull function with different values of the shape parameter: Probability Density Function (left), Cumulative Distribution Function (right).

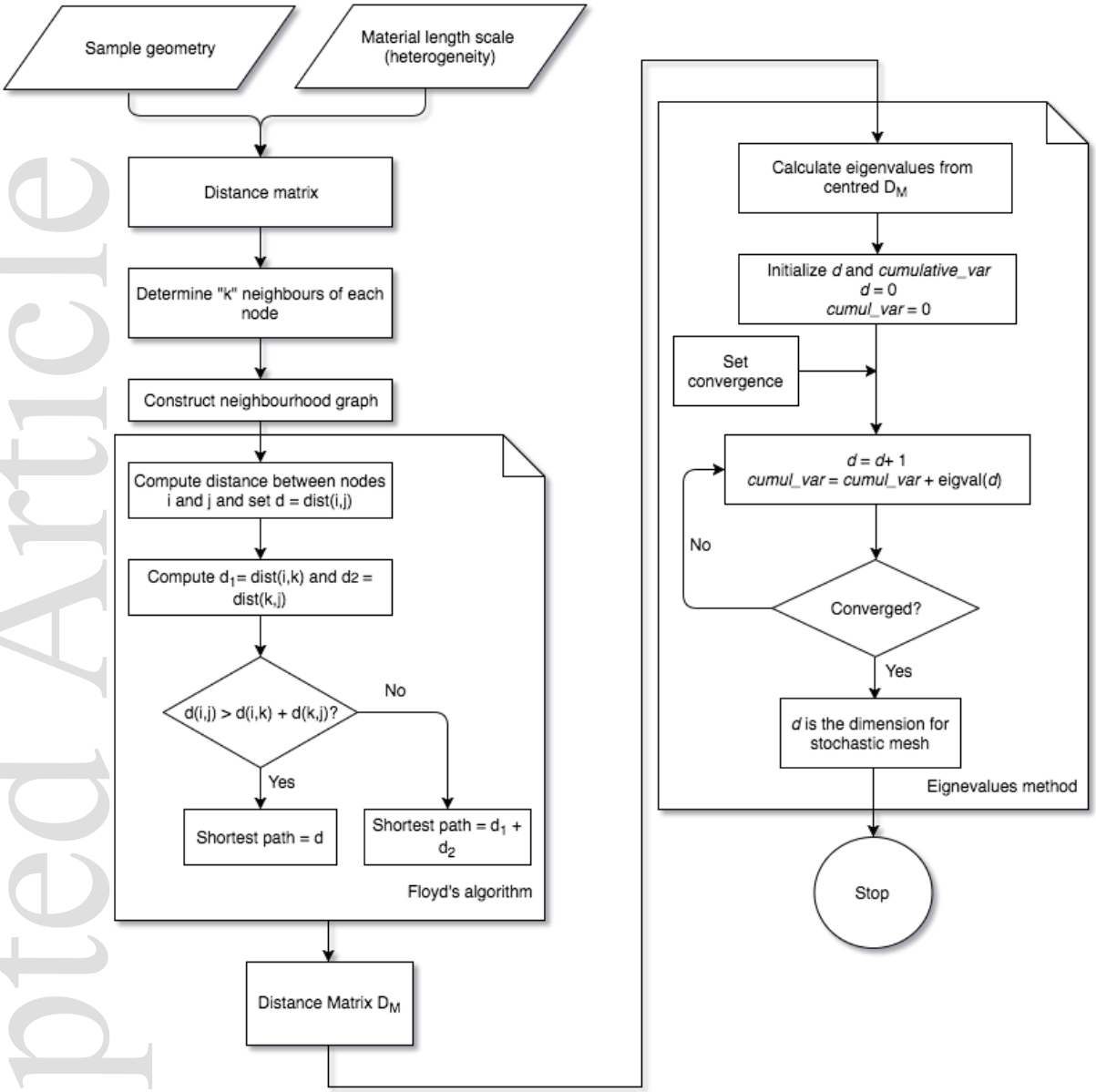

Figure 2. Algorithm for IsoMap

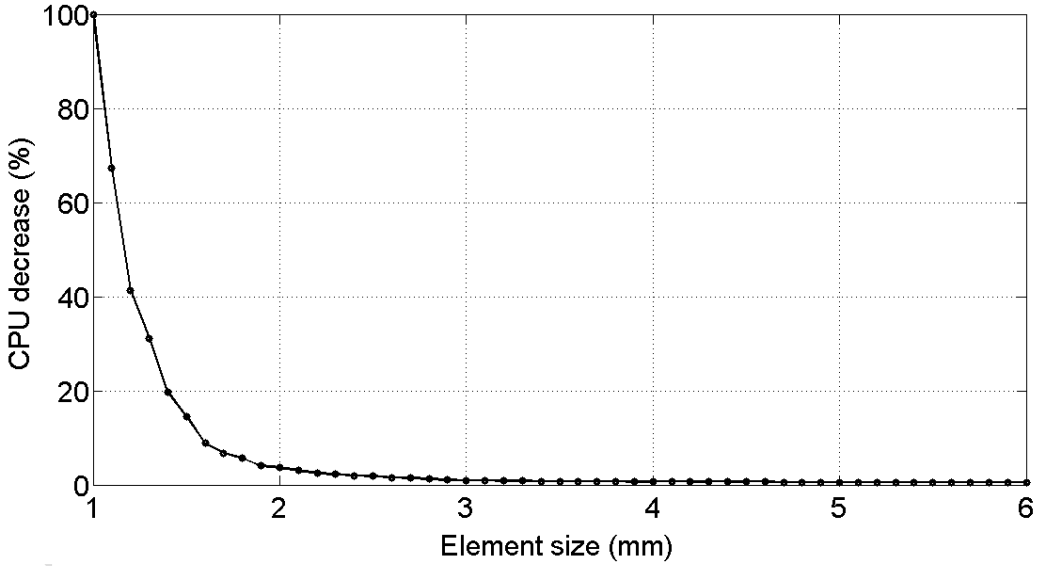

Figure 3. Sample generation: CPU evolution for different stochastic element sizes on the same problem. An increase in the size of the mesh leads to a reduction of the CPU time needed for the process. However, an excessive increase for the mesh size doesn't lead to any significant improvement.

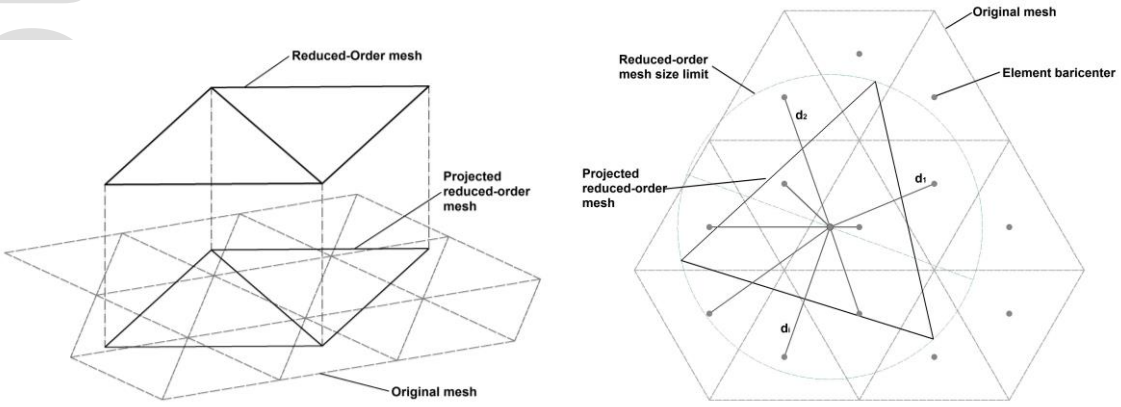

Figure 4. Mapping procedure from stochastic to finite element mesh: projection of one mesh on the other (left) and calculation of the distances between barycentre (right). The new value of the random properties for the original finite element mesh is given by an average of the elements included within the projection, averaged according to the relative position between the elements.

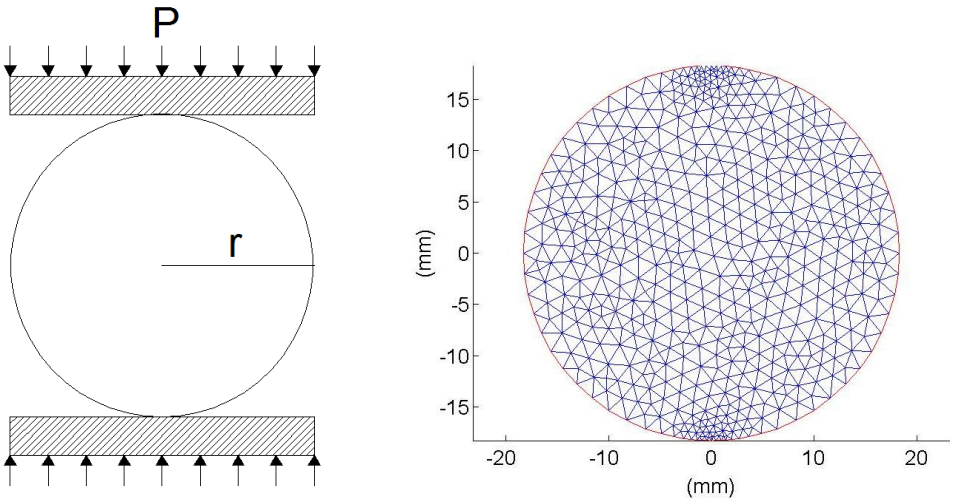

(a) **(b)**

Figure 5. a) Geometry, boundary and loading conditions of the rock sample; b) two-dimensional finite element mesh.

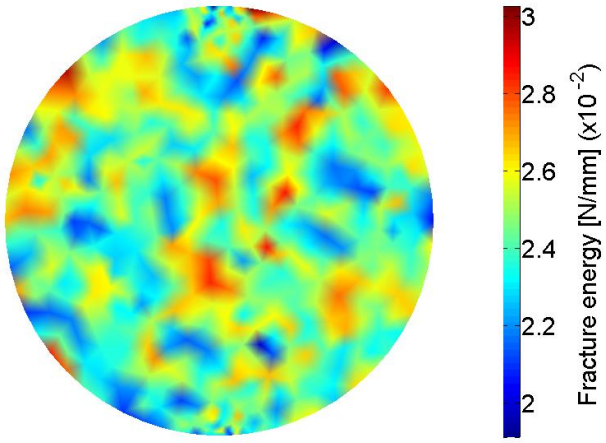

Figure 6. A realization of the randomly distributed fracture energy in the cylindrical disc.

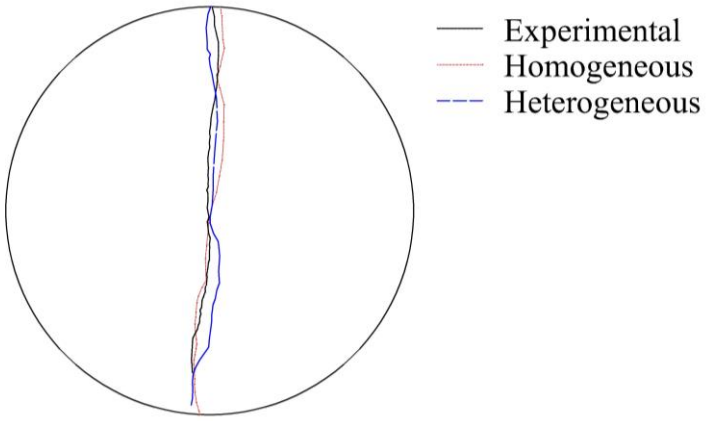

Figure 7. Comparison between crack paths achieved with homogeneous, one of the heterogeneous models and experiment.

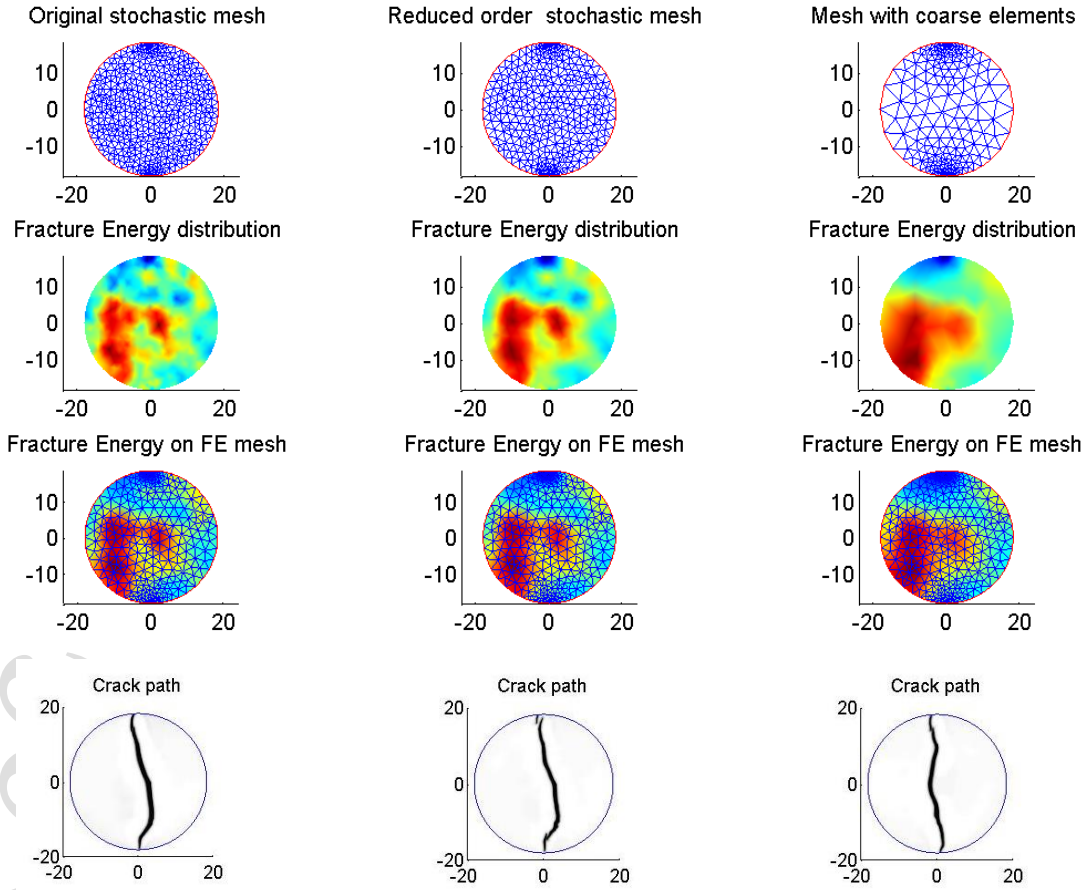

Figure 8. Comparison between original stochastic mesh (left column), reduced-order stochastic mesh with correct size (central column) and excessive dimension (right column). The dimension of the reduced-order stochastic mesh is related to the size of its neighbourhood. With a very small neighbourhood size, the size of the mesh increases, leading to a loss of information of the stochastic field. This causes the predicted crack path to be significantly different from the original one. With an adequate dimension of the neighbourhood, crack path is still very close to the initial one.

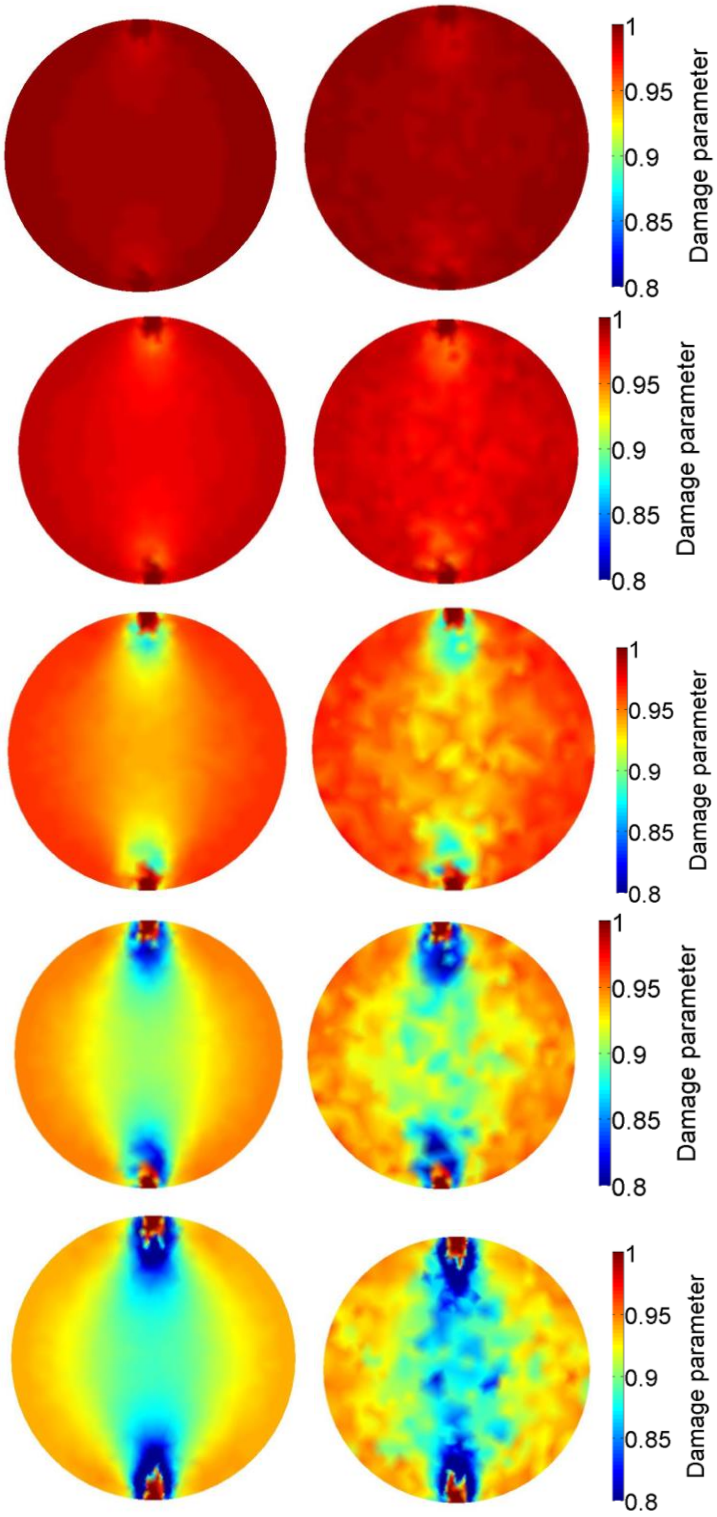

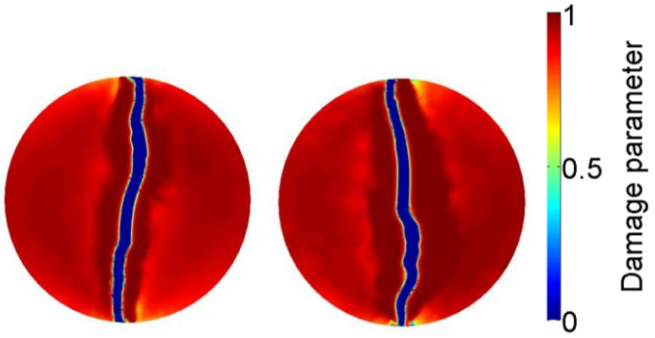

Figure 9. Evolution of damage state in the disc for homogeneous (left) and one of the heterogeneous models with unit standard deviation (right).

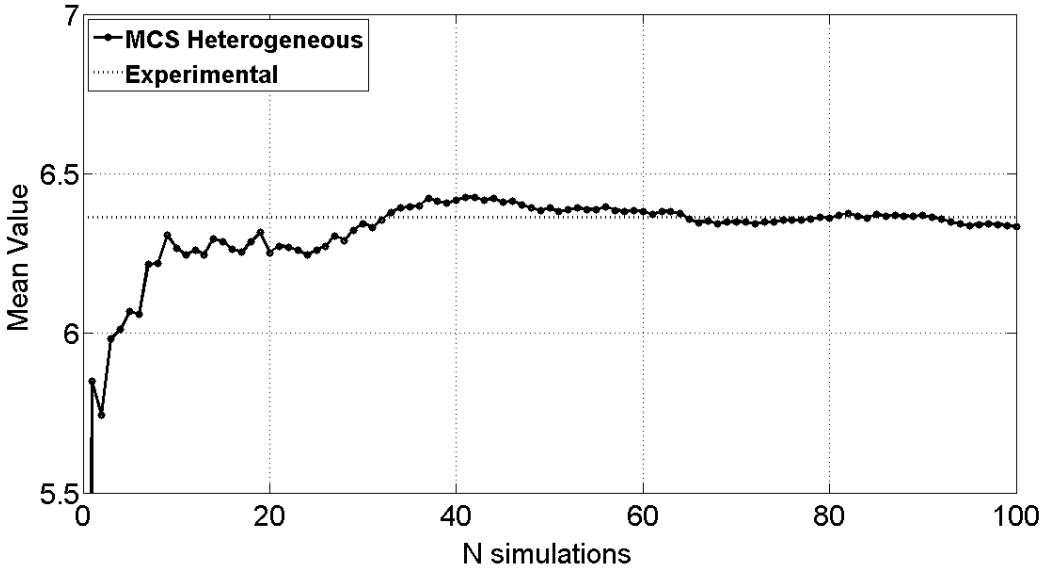

Figure 10. Brazilian disc test: Convergence of calculated mean value of tensile strength from simulations and comparison with tensile strength obtained from experiment for unit standard deviation.

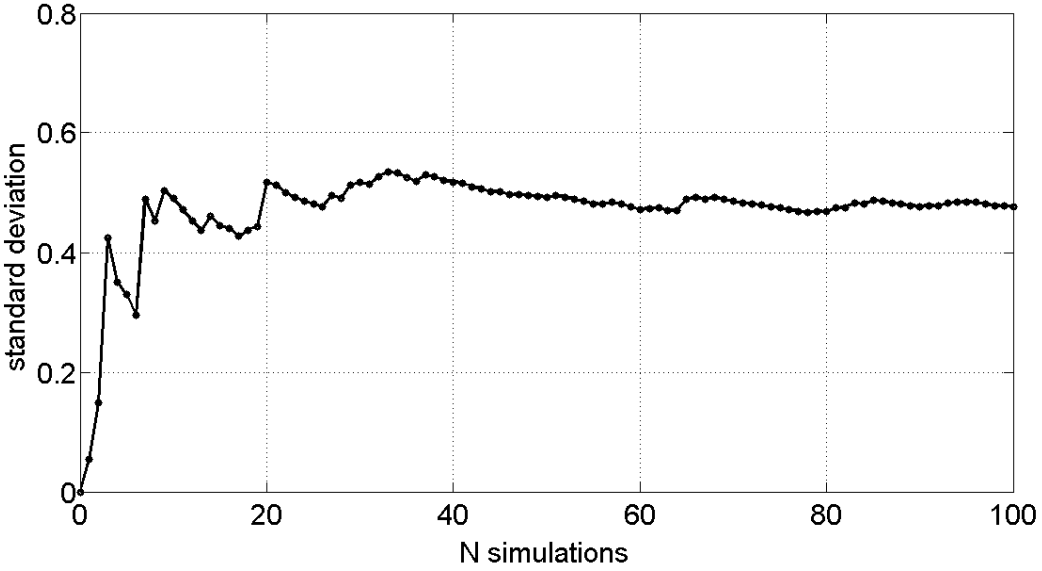

Figure 11. Brazilian disc test: Effect of the number of MC simulation samples on the standard deviation of the tensile strength for unit standard deviation. Standard deviation's trend gets stable after about 65 simulations.

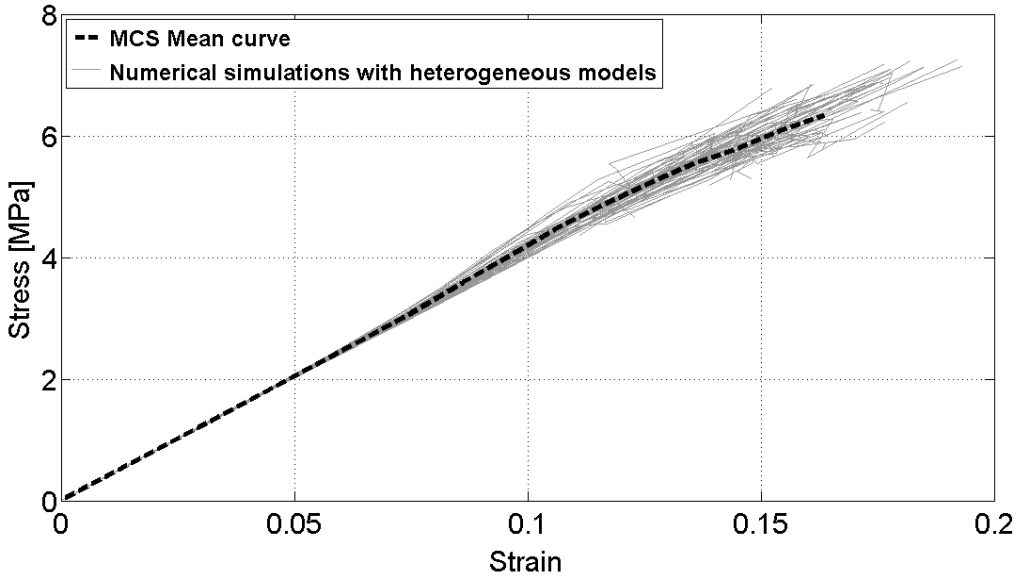

Figure 12. Brazilian disc test: Stress-Strain curves for 100 simulations and mean stress-strain curve.

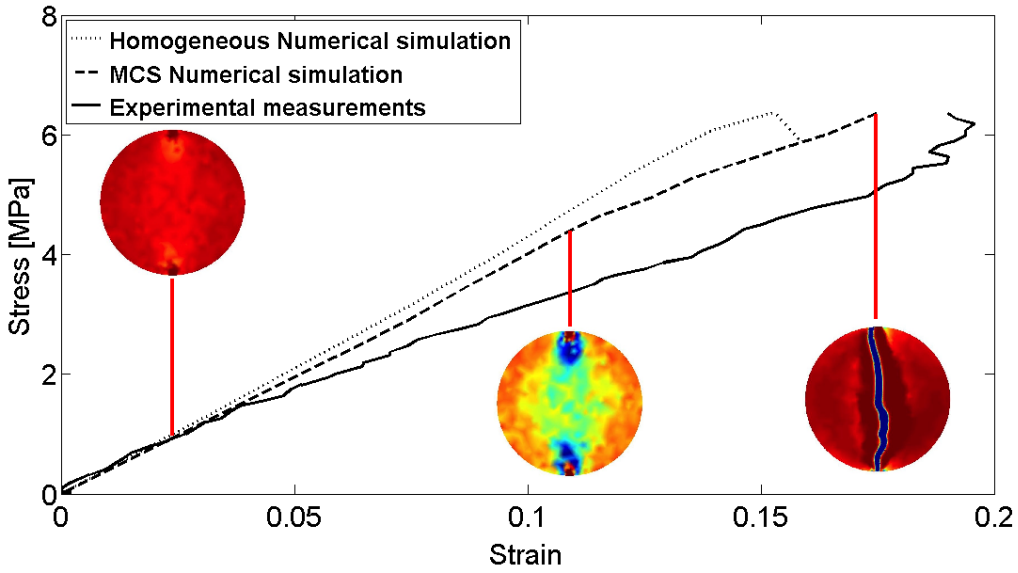

Figure 13. Brazilian disc test: stress-strain curves, comparison between experimental data and numerical results from homogeneous and heterogeneous models for unit standard deviation.

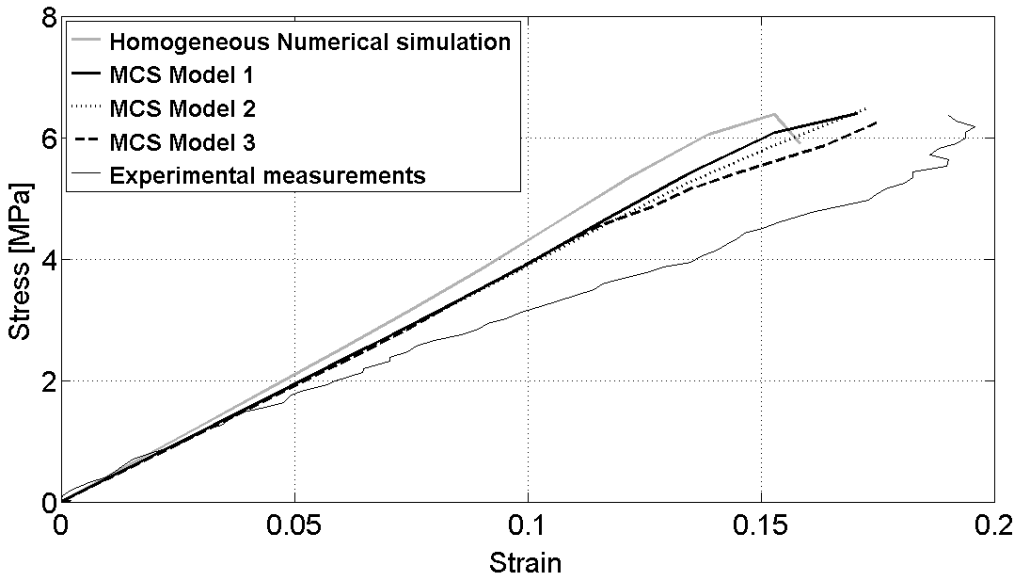

Figure 14. Brazilian disc test: stress-strain curves, comparison between experimental data and numerical results from homogeneous and heterogeneous models with different values of standard deviation: (model 1) 0.1 x 10^{-3}; (model 2) 0.5 x 10^{-3}; (model 3) 1 x 10^{-3}.

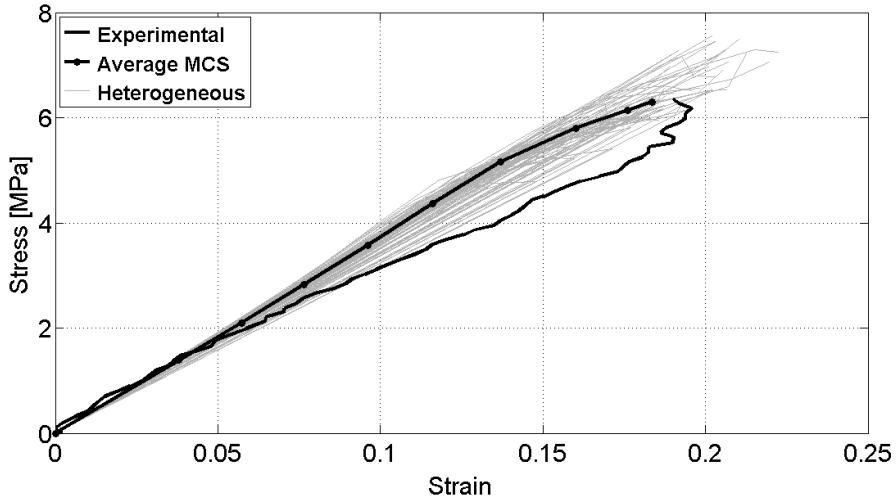

(a)

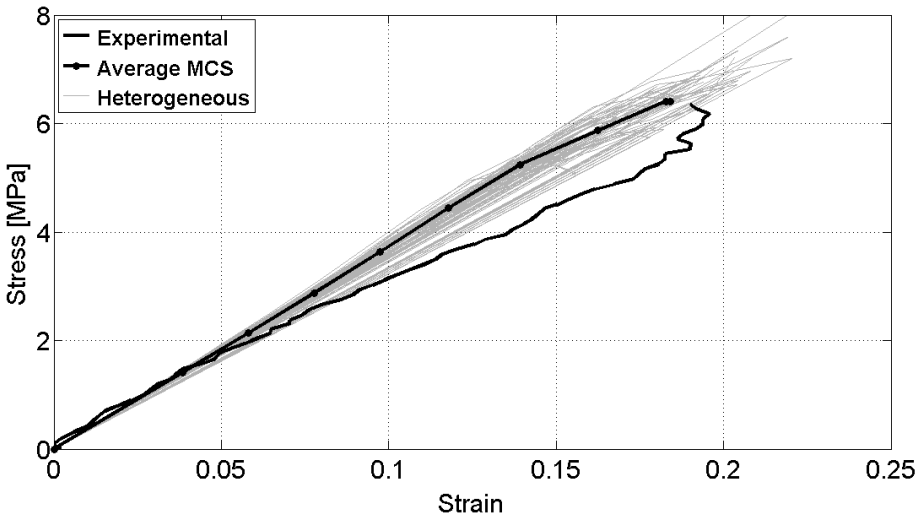

(b)

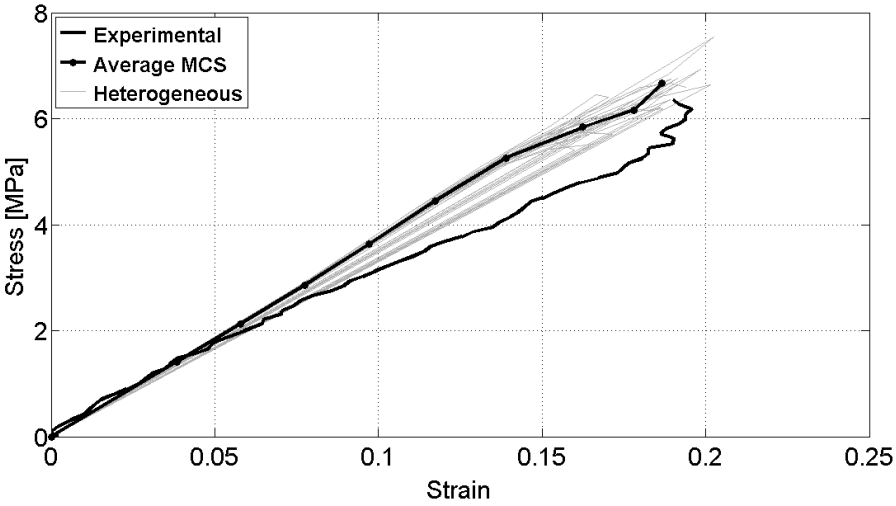

(c)

Figure 15. Brazilian disc test: stress – strain plots obtained from MC simulation for three different degrees of correlation. (a) full correlation, (b) partial correlation and (c) no correlation between fracture energy and modulus of elasticity.

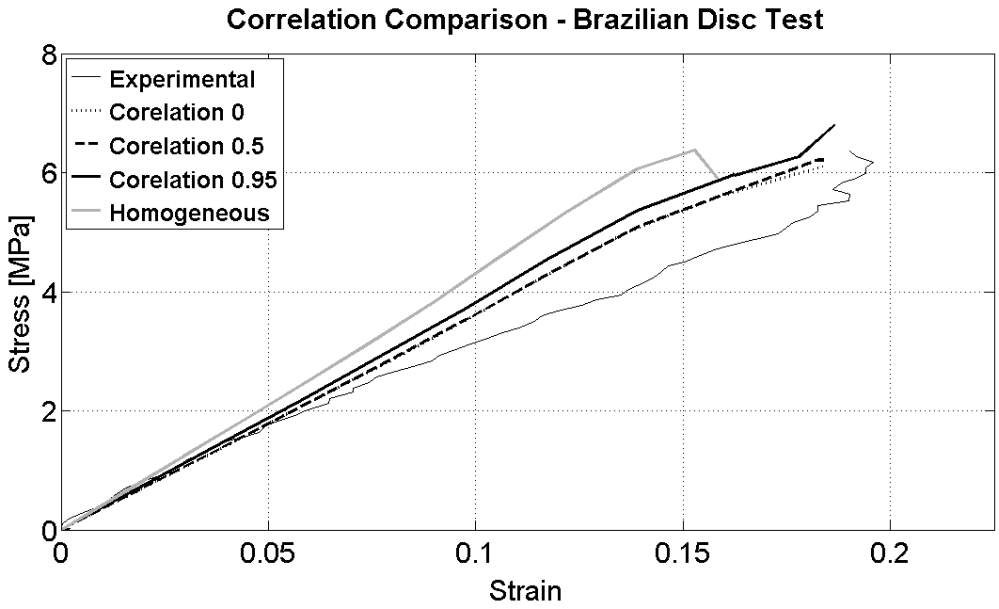

Figure 16. Brazilian disc test: Comparison between the stress – strain curves obtained from MC simulation for three different degrees of correlation.

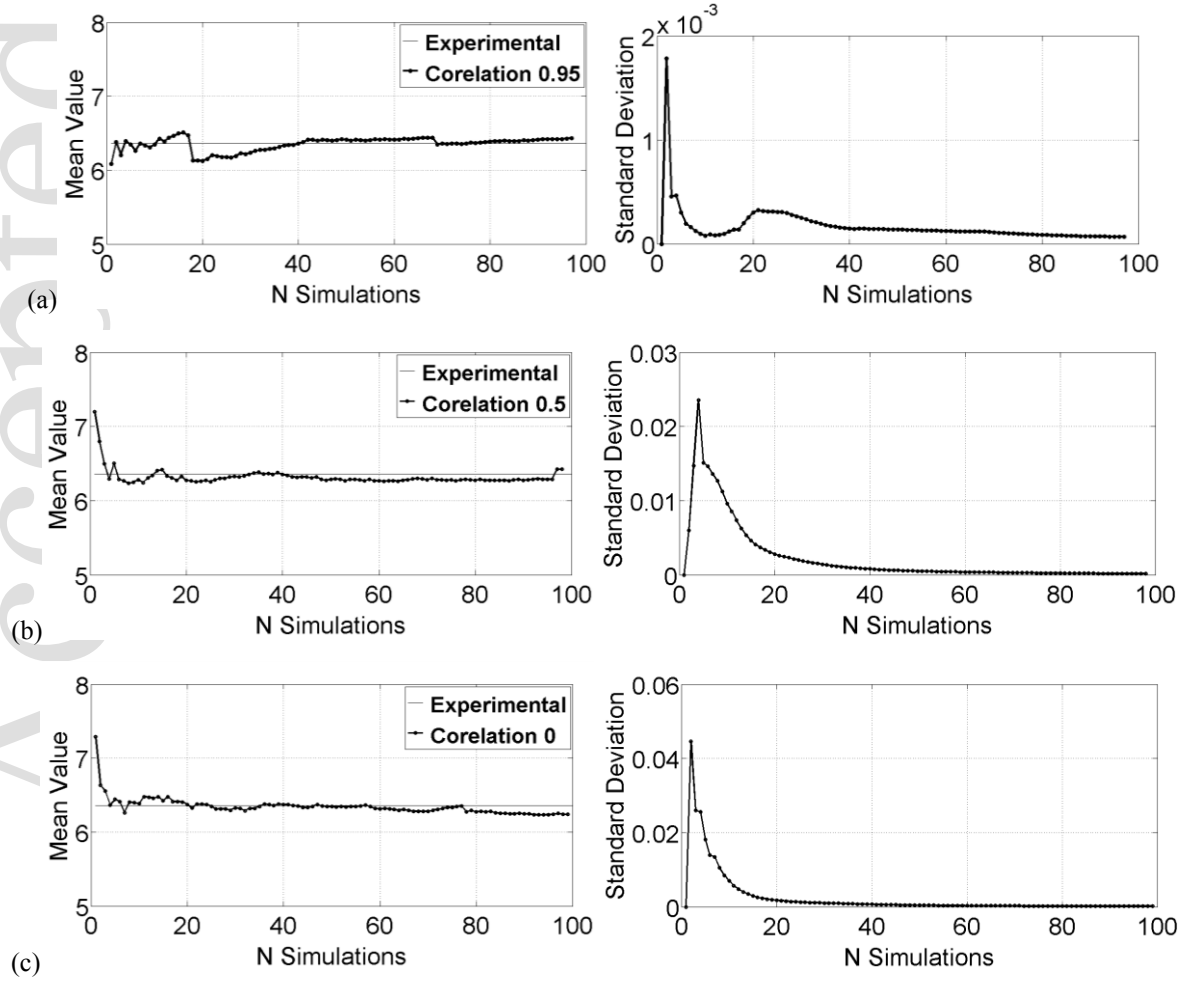

Figure 17. Brazilian disc test: convergence of the mean value and standard deviation of the stress obtained from simulations with different degree of correlation. (a) full correlation, (b) partial correlation and (c) no correlation, between fracture energy and modulus of elasticity.

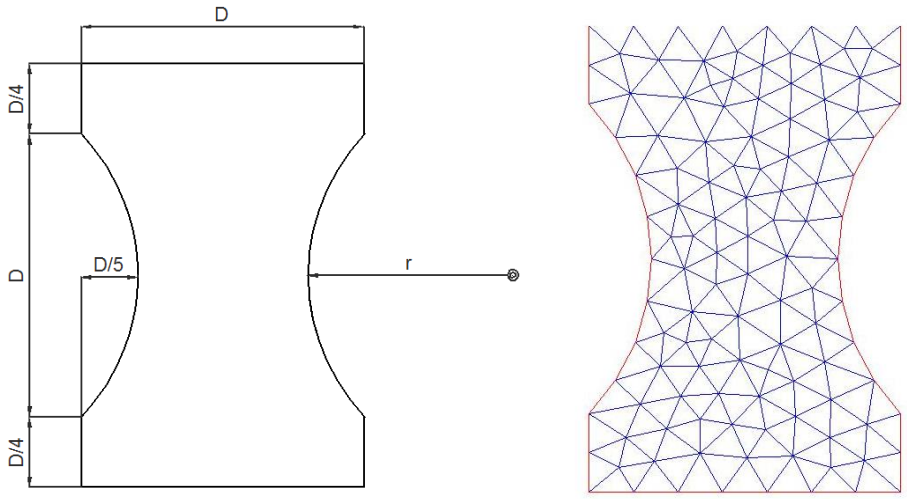

Figure 18. Dog bone specimen: geometry definition with D = 50 mm, r = 36. 53 mm and thickness = 100 mm (left) and Finite Element discretization (right)

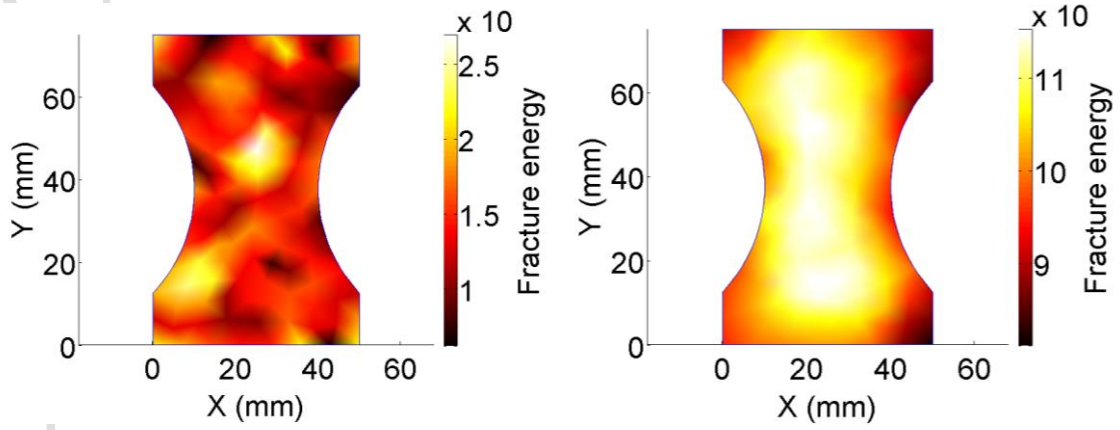

Figure 19. Dog bone specimen: Randomly selected realizations for standard deviation $5x10^{-2}$ and correlation length of 1.2 (left) and 15 (rigth) mm

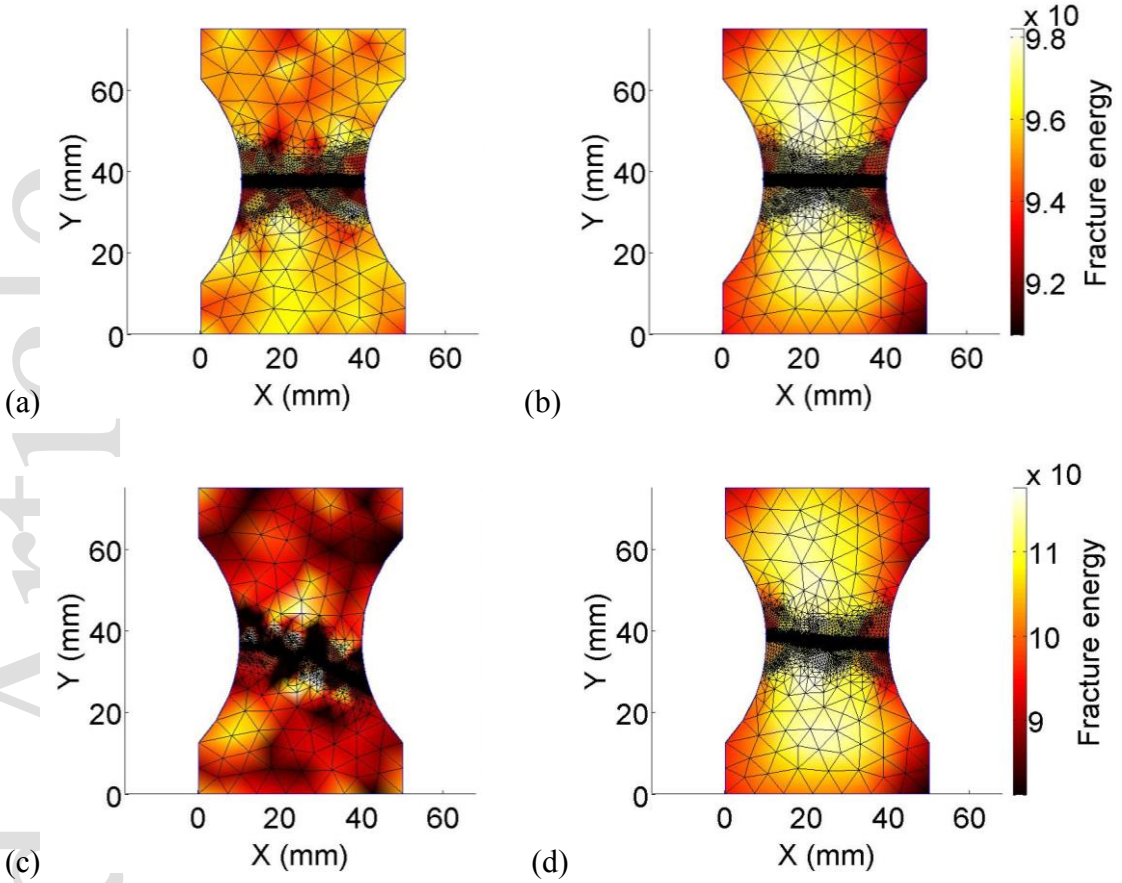

Figure 20. Dog bone specimen: crack paths for randomly selected realization and for different values of correlation length and standard deviation. (a) l_c = 1.2, Std Dev $0.1x10^{-2}$; (b) l_c = 15, Std Dev $0.1x10^{-2}$; (c) l_c = 1.2, Std Dev $5x10^{-2}$; (d) l_c = 15, Std Dev $5x10^{-2}$.

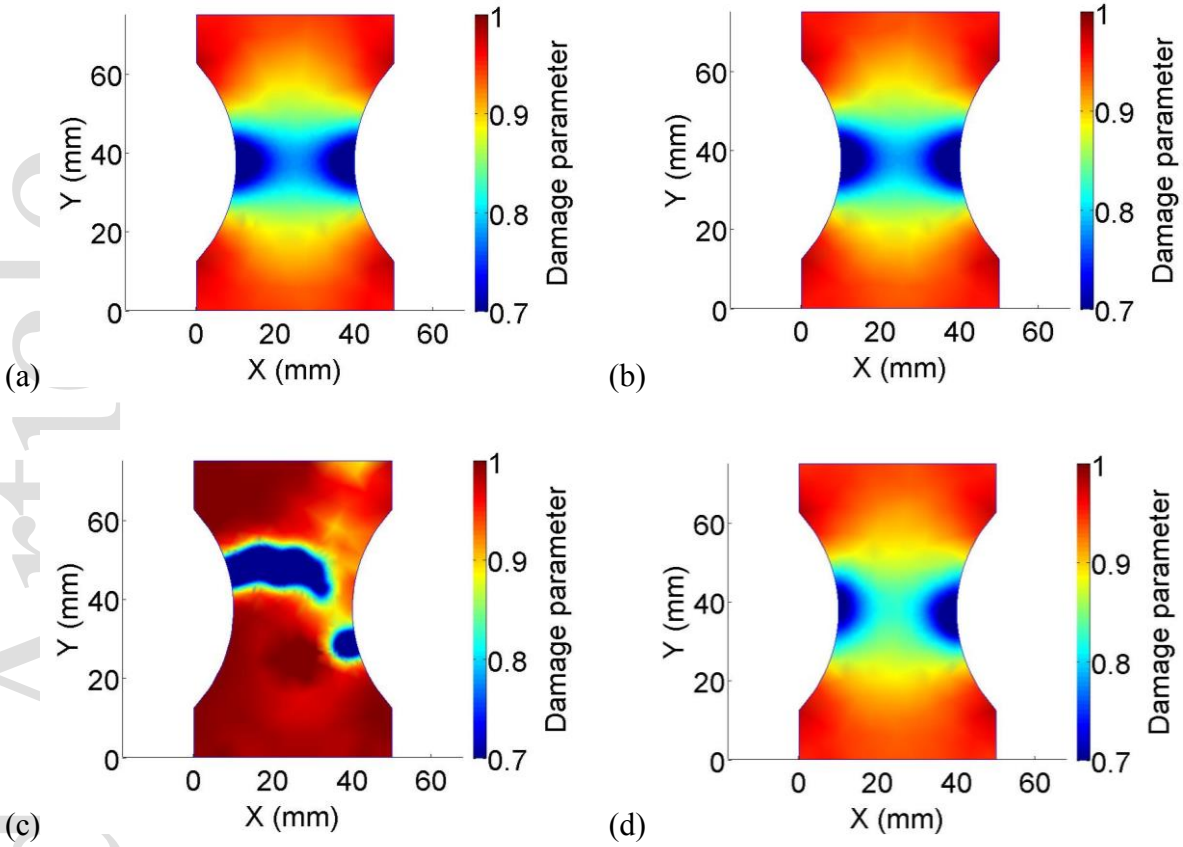

Figure 21. Dog bone specimen: damage distribution over the specimen for randomly selected realization and for different values of correlation length and standard deviation. (a) l_c = 1.2, Std Dev $0.1x10^{-2}$; (b) l_c = 15, Std Dev $0.1x10^{-2}$; (c) l_c = 1.2, Std Dev $5x10^{-2}$; (d) l_c = 15, Std Dev $5x10^{-2}$.

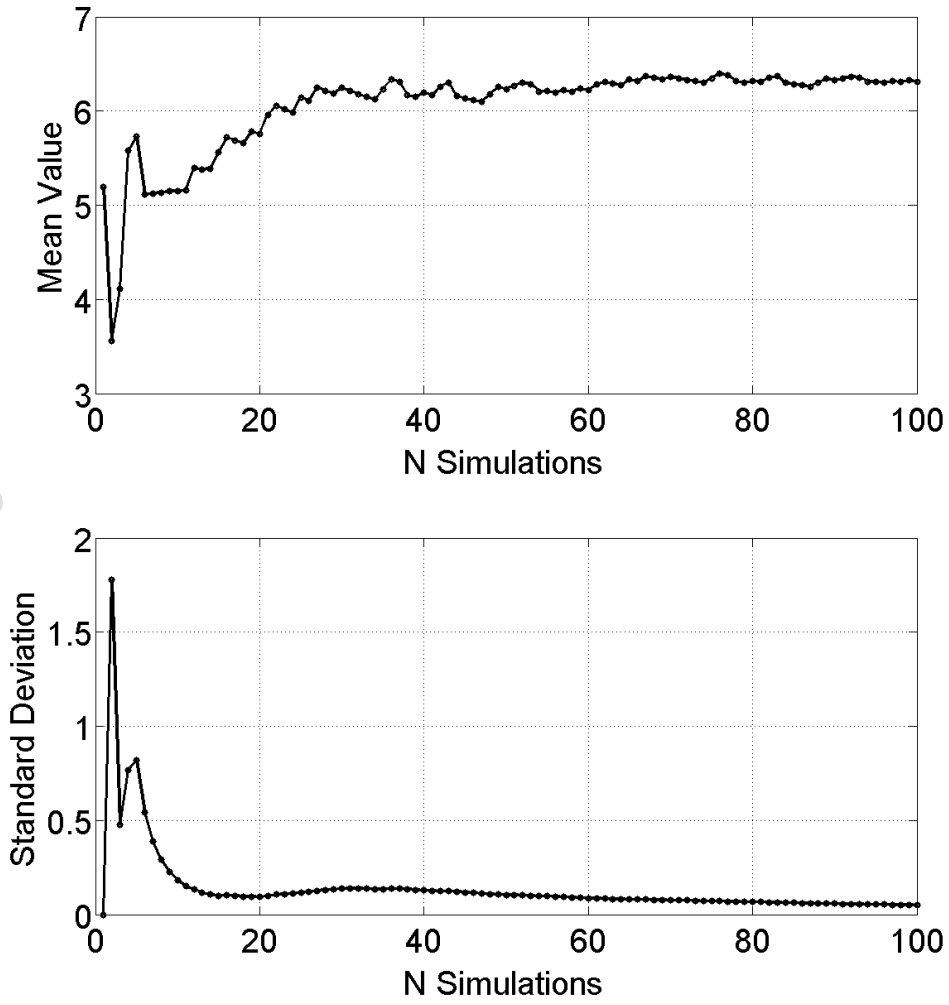

Figure 22. Dog bone specimen: convergence for mean (top) and standard deviation (bottom) of the peak load (stochastic fracture energy with standard deviation $5x10^{-2}$ and correlation length 1.2)

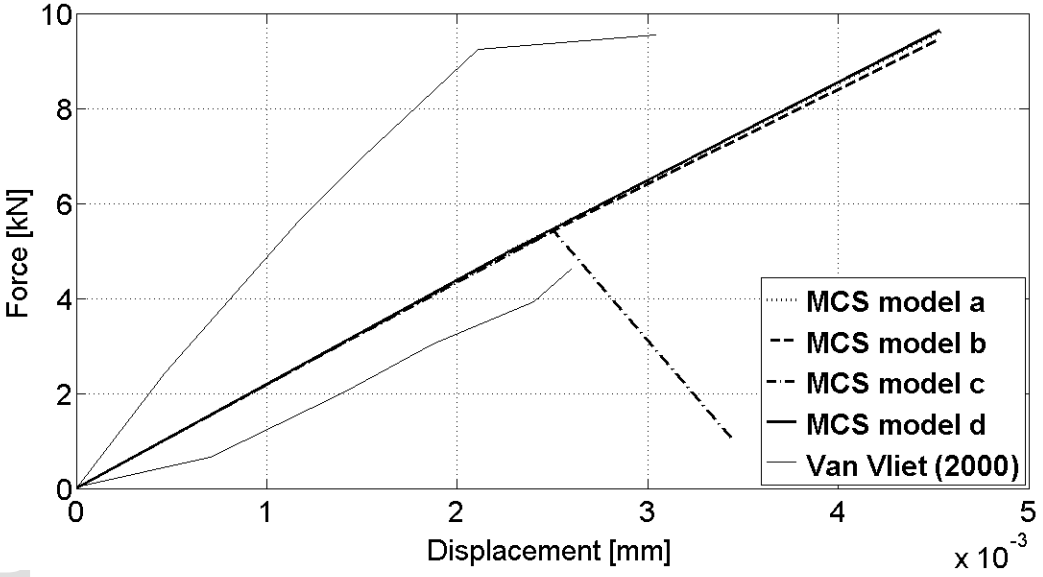

Figure 23. Dog bone specimen: load – displacements curves for different values of correlation length and standard deviation. (model a) l_c = 1.2, Std Dev 0.1x10^{-2}; (model b) l_c = 15, Std Dev 0.1x10^{-2}; (model c) l_c = 1.2, Std Dev 5x10^{-2}; (model d) l_c = 15, Std Dev 5x10^{-2}.

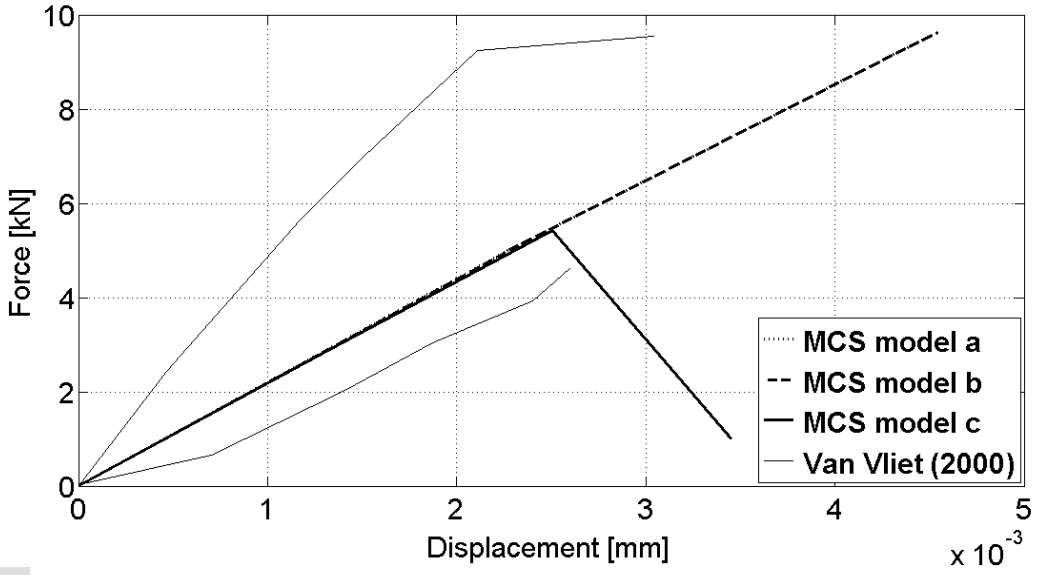

Figure 24. Dog bone specimen: load – displacements curves for l_c = 1.2 and different values of standard deviation: (model a) standard deviation 0.5x10^{-2}; (model b) standard deviation 1x10^{-2}; (model c) standard deviation 5x10^{-2}.

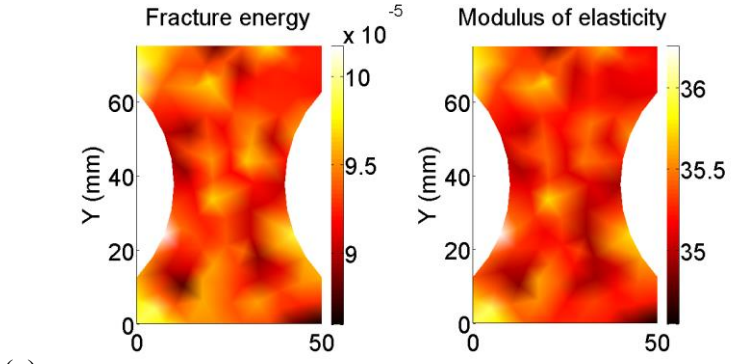

(a)

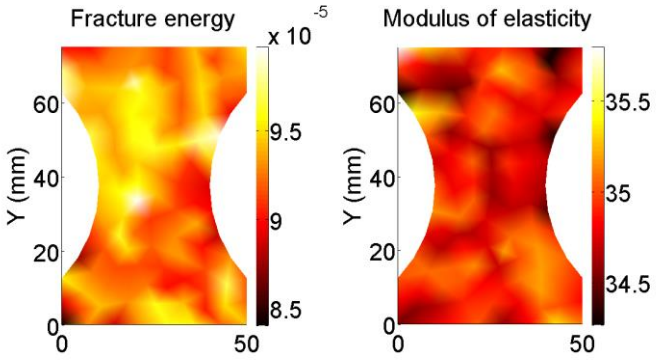

(b)

Figure 25. Dog bone specimen: randomly selected realizations for fracture energy and modulus of elasticity in case of full correlation (a) and no correlation (b) between variables.

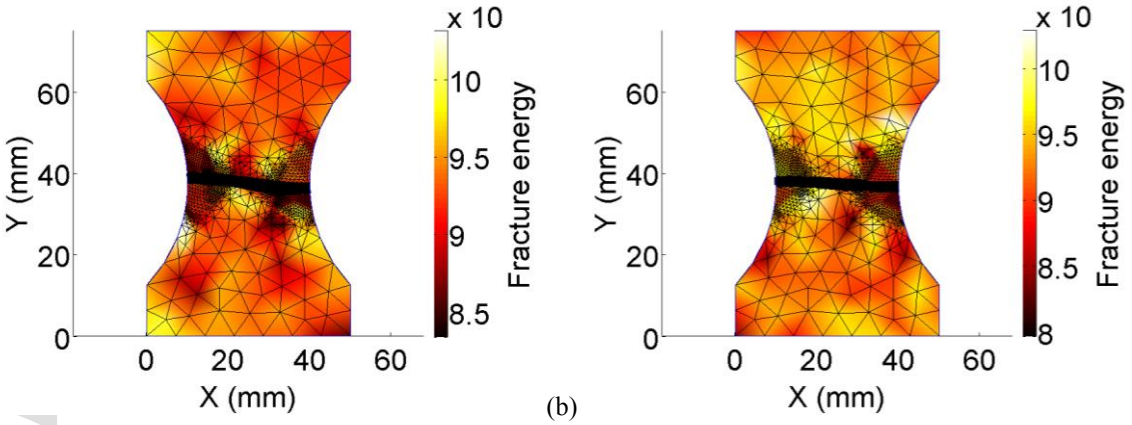

(a)

(b)

Figure 26. Dog bone specimen: crack paths for randomly selected realization and for different values of cross correlation between fracture energy and modulus of elasticity. (a) fully correlated variables (b) uncorrelated variables.

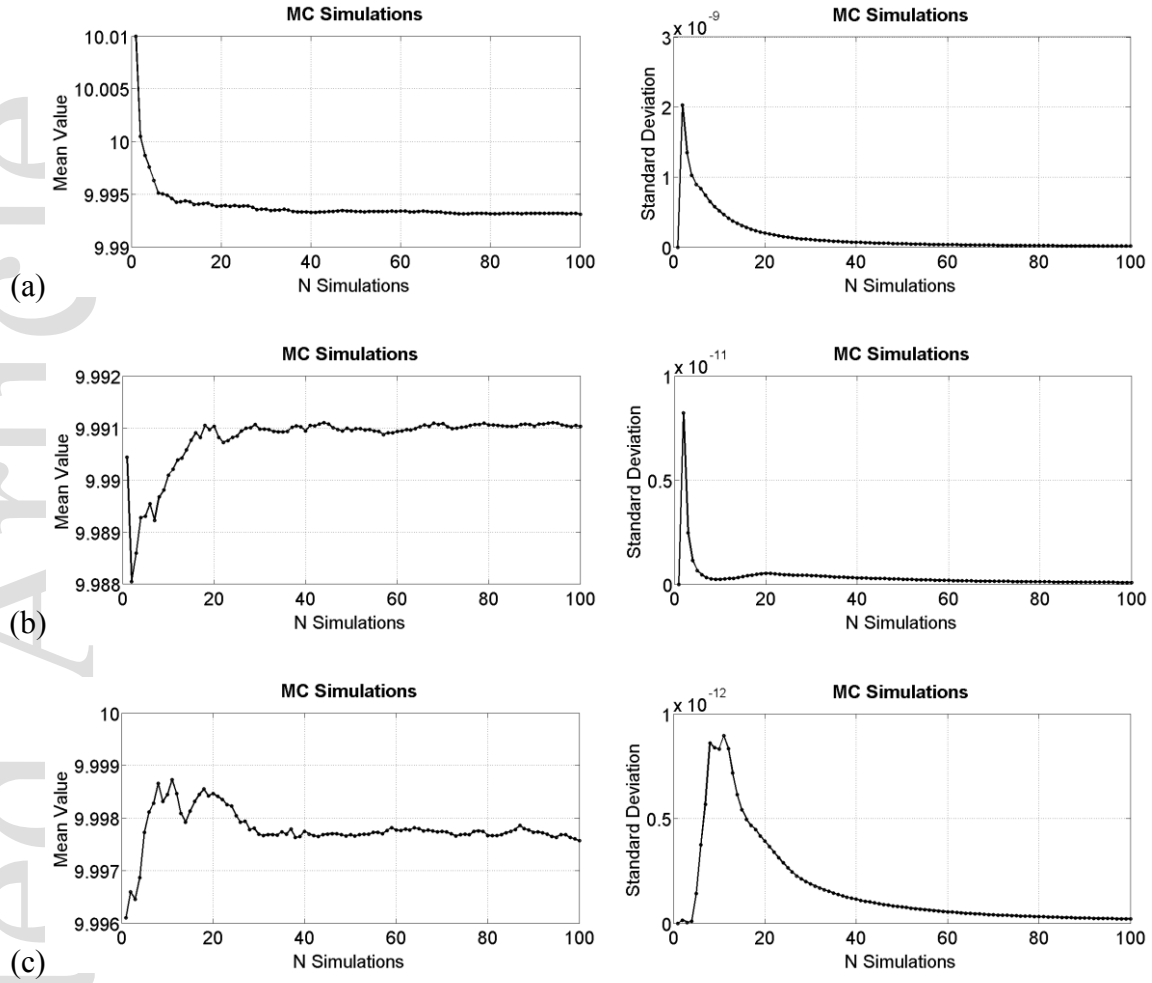

Figure 27. Dog bone specimen: convergence for mean (left) and standard deviation (right) of the peak load for different degrees of cross correlation. (a) fully correlated, (b) partially correlated and (c) uncorrelated variables.

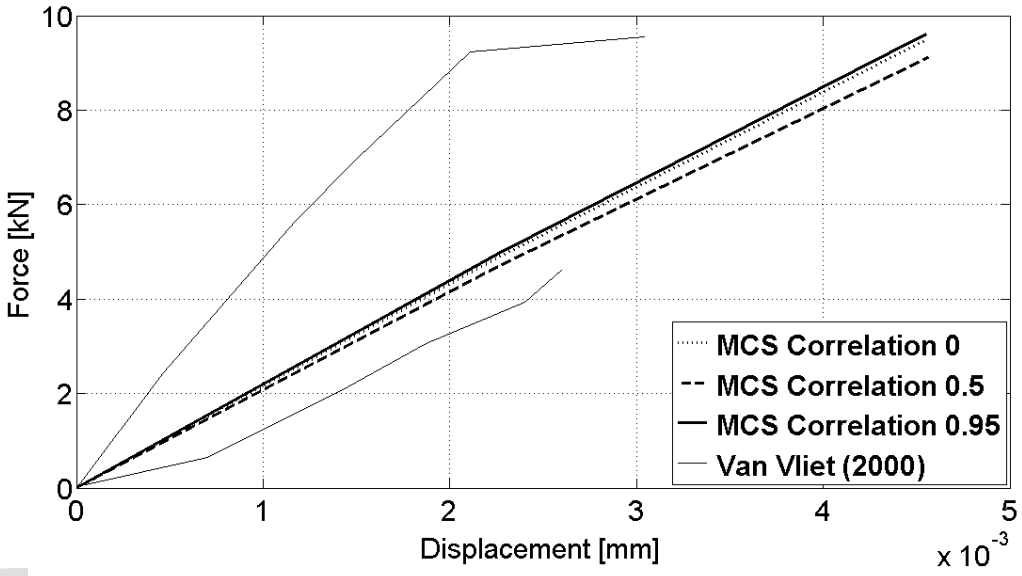

Figure 28. Load – displacements plot for the dog bone specimen for realization with different values of cross-correlation.